A Review of Technical Aspects and Challenges in Opportunistic Rainfall Estimation Using Satellite and Terrestrial Microwave Links

How wireless infrastructure can be used for rainfall monitoring

ROBERTO NEBULONI, FILIPPO GIANNETTI, FABIOLA SAPIENZA, VINCENZO LOTTICI, ELISA ADIROSI, GIACOMO ROVERSI, ELIA COVI, CHRISTIAN GIANOGLIO, MATTEO COLLI, AND CARLO DE MICHELE

©SHUTTERSTOCK.COM/AAPSKY

The idea of using terrestrial or satellite microwave links (SMLs) as opportunistic sensors (OSs) of rainfall is more than 15 years old, and the literature on the topic is vast. Many studies focused on rain detection and quantification from the data collected by the fronthauling and backhauling links of mobile networks, namely, commercial microwave links (CMLs). More recently, several researchers have also investigated the signals received by the ground terminals of TV-SAT or Internet of Things (IoT) satellite-based service subscribers, namely SMLs. CMLs and SMLs have different characteristics from those of conventional sensors (CSs) of rainfall; hence, they have the potential to complement measurements collected by rain gauges (RGs) or weather radars (WRs) as well as to provide unique data in the several areas of the globe where rainfall monitoring systems are scarce or completely missing. Unlike previous reviews on the topic, this work aims to survey the technical challenges involved by the usage of devices and data not designed for rainfall monitoring. In particular, we draw a state-of-the-art flowchart of OS data processing, we analyze the disturbances that affect the raw data, and we then present a comparative analysis of the major studies on the validation of OS rainfall estimates, based on a set of key performance indicators (KPIs). The similarities and differences of satellite and terrestrial links as rainfall sensors are highlighted. To conclude, we propose an author's view on the future of rainfall measurements by CMLs and SMLs, which is closely tied to the evolution of wireless communication networks.

INTRODUCTION

Quantitative precipitation estimation is crucial for a broad spectrum of applications, including meteorology [1], climatology [2], weather forecasting [3], hydrology [4], and water management [5]. Today, networks of RGs [6] and WRs [7],

Digital Object Identifier 10.1109/MGRS.2025.3573645
Date of publication 1 August 2025; date of current version 11 December 2025.

[8] are the key instruments for measuring precipitation at an operational level. Additionally, Earth observation satellites provide precipitation products over large areas [9], although with a lower spatial and temporal resolution. Furthermore, disdrometers are increasingly used as they are able to measure the size and velocity of falling raindrops [10]. Several applications require small-scale measurements and fast sampling [11] to track localized and rapidly evolving severe rainfall events, which are increasingly more frequent as an effect of climate change. The required resolution of rainfall measurements can be in the order of 10 km, down to 100 m (in space) and 10 min, down to 1 min (in time). However, current operational networks of rain sensors cannot provide this performance everywhere.

NOMENCLATURE

AI	artificial intelligence
ANN	artificial neural network
ATPC	automatic transmit power control
CCDF	complementary cumulative distribution function
CML	commercial microwave link
CNN	convolutional neural network
COTS	commercial off-the-shelf
CS	conventional sensor
CV	coefficient of variation
DSD	drop size distribution
DTH	direct to home
DVB-S/S2	Digital Video Broadcasting - Satellite/Satellite second generation
FT	fast tracker
GEO	geostationary Earth orbit
HM	harmonic mean
IF	intermediate frequency
IPL	ice particle layer
KPI	key performance indicator
LEO	low-Earth orbit
LL	liquid layer
LNB	low-noise block
LSTM	long short-term memory
LWC	liquid water content
MBE	mean bias error
MCC	Matthews correlation coefficient
MDE	mean detection error
ML	melting layer
MNO	mobile network operator
NMAE	normalized mean absolute error
NRMSE	normalized bias-corrected root-mean-square error
OS	opportunistic sensor
PCC	Pearson correlation coefficient
PSD	particle size distribution
RB	relative bias
RF	radio frequency
RG	rain gauge
RMSE	root-mean-square error
$\mathbf{RMSE_r}$	root mean square of relative error
RSL	received signal level
SML	satellite microwave link
SNR	signal-to-noise ratio
ST	slow tracker
SVM	support vector machine
TBRG	tipping-bucket rain gauge
TSL	transmitted signal level
WAA	wet antenna attenuation
WR	weather radar

In addition to the previously listed instruments, referred to as CSs, new opportunities are opening up, thanks to the growth of wireless telecommunication networks worldwide. Indeed, any terrestrial or satellite-to-ground link operating at a frequency that is sensitive to rainfall (roughly, above 5 GHz) is, in principle, an OS of precipitation, provided that the time series of the received signal level (RSL) are collected and stored by the system. The RSL can be either the received power or some equivalent quantity, such as the signal-to-noise ratio (SNR). Examples are the backhauling links of terrestrial cellular networks, hereinafter called CMLs, or the downlinks of direct-to-home (DTH) satellite broadcasting, namely SMLs. A schematic overview of the main technical characteristics of CSs and OSs is shown in Table 1 to highlight the main differences in terms of frequency range, collected variables, spatial and temporal resolutions, and economic costs.

Opportunistic sensing of precipitation through CMLs and SMLs has several advantages:

- In many low-income countries, networks of WRs are not available, and RGs are scarce [12] because of their high installation and maintenance costs. In addition, providing free access to these data is challenging [13]. On the other hand, the ubiquitous growth of wireless communications turned OSs into a solution for the quick deployment of rain sensing networks in these countries [14], [15], [16], [17].

- Where RGs or WRs are already in place, OSs represent an efficient and low-cost solution to complement the operational networks of CSs, filling gaps or improving coverage [18]. Moreover, merging OS and CS data or different types of OS data can significantly improve the accuracy of rainfall estimates [19], [20].
- CML and SML microwave receivers are able to collect rainfall data with a fine temporal resolution, that is, in the order of 1 min [21], [22], [23], [24]. Moreover, precipitation is observed by OSs along a straight line corresponding to the propagation path of the electromagnetic wave [25], [26]. The combination of high resolution in time and spatial sampling capability as well as the availability of dense networks of sensors (in the case of CMLs) results in a more effective measurement of the spatial distribution of rainfall intensity than that obtained with RGs [18].

In the following sections, "CSs" and "Oss," CSs and OSs are briefly reviewed, while the section "Outline of This Work" summarizes the major contributions of this review.

CSs

Ground-based RGs, such as the plain old tipping-bucket rain gauge (TBRG) or the more advanced weighing-type gauge, are relatively simple sensors and are currently the primary reference for rainfall measurements [6]. Standards for the accuracy of RG measurements are provided by the recommendations of the World Meteorological Organization [27]. RGs are point-based devices with a small capture area (usually less than 1,000 cm^2), which is a major limitation when evaluating the spatial variability of rainfall is important. Moreover, TBRGs are known to underestimate at heavy rainfall intensities [28] or in the presence of wind [29].

Disdrometers are another type of point sensor [10], [30], [31]. They are able to measure the microphysical properties of precipitation, such as the particle size distribution (PSD), which is important for several applications. It is known that disdrometers may undercount small drops with diameters smaller than about 0.3 mm [10]. In addition, disdrometer measurements are affected by the presence of wind, which results in a bias of the measured PSD [32], [33].

Ground-based WRs provide broad spatial coverage—up to 150 km—as well as high spatial and temporal resolutions, i.e., in the order of 1 km in space and 5–10 min in time, respectively [7]. However, they provide indirect measurements of precipitation [34] collected aloft rather than at ground level, and they are not immune to measurement

TABLE 1. COMPARISON OF THE KEY FEATURES OF CSs AND OSs.

	CS			OS	
SENSOR	**WR**	**RG**	**DISDROMETER**	**CML**	**SML**
Frequency range	2–10 GHz[a]	–	Infrared or visible	6–42 GHz[b] 71–76 GHz[d] 81–86 GHz[d]	10.7–12.75 GHz[c] 17.7–21.2 GHz[e]
Measured variables	- Reflectivity - Doppler velocity - Polarimetric variables	Cumulated rain	- Particle fall velocity - Particle size	Path attenuation	
Primary geophysical variables	- Precipitation intensity - Hydrometeor classification	Cumulated rain	- PSD - Precipitation intensity - Precipitation type	Precipitation intensity	
Spatial sampling	Over volumes	Point-based sensor		Over a straight line (terrestrial path)	Over a straight line (space-to-Earth path)
Spatial resolution (single sensor)	1 km × 1 km[f]	N/A		N/A[g]	
Spatial resolution (networks of sensors)	1 km × 1 km	Average distance between sensors			
Temporal resolution	5–10 min	1–30 min	1 min (typical)	10 s–15 min	30 s–15 min
Cost (single sensor)[h]	€150,000–1 million (X-band)[a] €1.5 million–3.5 million (C-band)[a] €3 million–8 million (S-band)[a]	€100–2,000	€3,000–70,000	Upon agreement with MNO	€100–1,000

PSD: particle size distribution; MNO: mobile network operator.
[a]Most widely used WR bands are S-band (2.7–2.9 GHz), C-band (5.25–5.725 GHz), and X-band (9.3–9.5 GHz).
[b]Noncontinuous allocations. This frequency range encompasses several microwave and millimeter-wave bands from C-band to Q-band.
[c]Ku band.
[d]E-band.
[e]Ka band.
[f]WR products are typically 2D maps of rainfall intensity at ground.
[g]CMLs and SMLs are often considered as point-based sensors located, for instance, midway through the path or at the ground terminal of an SML.
[h]Installation, maintenance, and operational costs are excluded here because they depend on many different variables. For CMLs, the cost is relative to the data, which are subject to an agreement with the MNO.

errors (e.g., miscalibration or attenuation effects). As a result, the capability of WRs to provide quantitative precipitation estimates remains an issue [34]. Furthermore, the coverage of ground-based radar can be limited in regions with a complex orography [35]. WRs on board satellites provide regional coverage and contribute to the understanding of large-scale precipitation processes. On the other hand, they have a much lower temporal resolution and a lower spatial resolution than ground-based radars [8]. For instance, the Dual-Frequency Precipitation radar on board the *Global Precipitation Measurement (GPM) Core* low-Earth orbit (LEO) satellite [36] has a 5 km × 5 km footprint and a revisit time of about four times per month. A higher temporal resolution is provided by the Integrated Multisatellite Retrievals for GPM product, which combines data from the different sensors on board the GPM satellite constellation [37]. Satellite products are obtained through complex algorithms and need continuous validation processes [38].

OSs

Wireless terrestrial links and Earth–satellite links operating in the microwave range of frequencies can be used as OSs of precipitation. The physical background is the same. Both rely on the decrease of the RSL while it is raining along the link, due to the absorption and scattering of the electromagnetic wave by the raindrops and referred to as rain attenuation [39]. Rain attenuation is directly related to the rainfall intensity along the propagation path. However, there are significant differences between CMLs and SMLs, including 1) the frequency bands allocated for satellite and terrestrial services (listed in Table 1), 2) the way in which raw data useful to precipitation estimation are generated and made available, 3) the way in which raw data are processed to derive precipitation estimates, and 4) the sources of disturbances affecting the RSL, which may impact the accuracy of precipitation estimates.

CMLs

CML refers to the wireless line-of-sight point-to-point terrestrial links that provide backhauling connectivity in mobile networks, i.e., the bridge between the radio access portion and the core of the network. Backhauling links transmit across licensed bandwidths in the frequency range of 6–42 GHz [40] over path lengths from a few hundreds of meters to a few tens of kilometers. Recently, very short E-band links (71–86 GHz) have been installed, especially in densely populated areas to support the increasing demand for high-capacity connectivity [41]. CMLs are designed to ensure extremely high link availability levels, typically in the order of 99.99% of the yearly time or even higher. To this aim, both the RSL and the transmitted signal level (TSL) of each link transceiver are continuously monitored. Rainfall intensity along the CML path can be retrieved from the raw data, i.e., the TSL and the RSL, and from the metadata. The metadata set includes (at least) the geographical position of the transceivers and the frequency and polarization of the signals. An important issue regarding CMLs is that mobile network operators (MNOs), that is, usually private companies, are the owners of the raw data. Moreover, the metadata are often classified as confidential; hence, they can be accessed only after signing nondisclosure agreements. Indeed, communication with MNOs and potential users, such as meteorological agencies, and the development of sustainable business plans are fundamental aspects to promote the exploitation of CML data [42].

WHERE RGs OR WRs ARE ALREADY IN PLACE, OSs REPRESENT AN EFFICIENT AND LOW-COST SOLUTION TO COMPLEMENT THE OPERATIONAL NETWORKS OF CSs, FILLING GAPS OR IMPROVING COVERAGE.

SMLs

The term SML refers to (at least) two different schemes based on Earth–space links, where the space terminal is usually a geostationary Earth orbit (GEO) satellite. One scheme relies on the signals conveying classical broadcasting services delivered by satellite operators, such as Digital Video Broadcasting - Satellite/Satellite second generation (DVB-S/S2) for TV-SAT. These signals can be measured by installing low-cost receivers [43], wherever the data collected by a network of such devices must be transferred to a server for processing. Unlike CML raw data, in this case, the opportunistic data are generated (and hence owned) by anybody able to install the receiving systems.

A different SML scheme is based on two-way Earth–space links, such as the ones for satellite-based IoT services or Internet via satellite [44]. The received power or the SNR measured by the ground receivers of the service subscribers is transmitted back to the gateway through the satellite, for instance, for link monitoring and data rate optimization. This scheme is similar to the one for CMLs since data are generated within the operational framework of the network, and they are managed by the satellite operator.

OUTLINE OF THIS WORK

This article reviews the technical aspects involved in the use of CMLs and SMLs as OSs of rainfall. Other important aspects, such as access to OS data and their availability for operational usage [22], standardization of data formats [45], and evolution of wireless networks, are beyond the scope of this contribution; hence, they are not investigated in depth here.

There are a few surveys in the literature on the topic of CMLs and SMLs. Some of them are rather general and touch on all of the previously discussed aspects [42], [46], while others are limited to either CMLs [47] or SMLs [26]. Unlike previous reviews, this work emphasizes signal impairments, physical limitations, and processing methodologies, filling the following gaps:

- It presents a general framework for OS data processing, highlighting the similarities and the differences between CML and SML data (in the section "Methodology for Rainfall Retrieval From OS Data").
- It provides a comparative analysis of the major works on rainfall identification and quantification by CMLs and SMLs (in the section "KPIs of OS Rainfall Estimation Accuracy").

This article has three specific objectives, which are addressed in the sections "Methodology for Rainfall Retrieval From OS Data," "A Broad Classification of Disturbances Affecting OS Signals," and "KPIs of OS Rainfall Estimation Accuracy," respectively. These objectives are

- giving an overview of the methods for converting CML and SML raw data into rainfall estimates
- discussing the disturbances that affect precipitation estimates obtained by CMLs and SMLs as well as their intrinsic limitations when used as precipitation sensors
- proposing a rationale as well as a set of KPIs to compare the performance of CML and SML data against those of CSs.

Conclusions and future trends are drawn in the final section. The ultimate goal of this review is to provide some recommendations and best practices, based on the current state of the art in the research, for the usage of OS data gathered from microwave links in the field of rainfall observation.

METHODOLOGY FOR RAINFALL RETRIEVAL FROM OS DATA

Methods for converting OS raw data into precipitation estimates (i.e., rainfall rate and rainfall accumulation) have been described in several articles in the literature (see e.g., [48] and [24] for CMLs or [49] and [50] for SMLs). Moreover, there are a few open software tools available for processing CML data, such as RAINLINK [51] or pycomlink [52]. Building on the research findings, we present a general framework for OS data processing, discussing the basic steps and highlighting the similarities and the differences between CMLs and SMLs.

The flowchart sketched in Figure 1 shows a general processing chain for retrieving rainfall intensity from CML or SML raw data. Hereafter, we briefly describe each block in the flowchart.

RSL MEASUREMENT AND SAMPLING

The receiver collects the RSL, i.e., the raw data, which consist of time series of the received power or of the SNR. The latter is defined as $\eta = E_s/N_0$, where E_s is the energy of the received radio-frequency (RF) signal (averaged over the duration of one digital modulation symbol) and N_0 is the one-sided power spectral density of the additive channel noise. RSL measurements are carried out within a given bandwidth at RF or at intermediate frequency (IF) after downconversion and sampled at a specified rate. Moreover, depending on the practical implementation of the receiver, the RSL can be either measured in analog form and subsequently digitized at a given sampling rate, or it can be obtained right in the digital domain using some signal processing algorithm applied to the samples of the received signal. In addition, the TSL (not shown in the figure) is often collected and made available in the case of CML. The two circular marks labeled CML and SML in Figure 1 indicate the starting points of the data processing flow for terrestrial and for satellite links, respectively, where the word "processing" means the conversion process of the raw data into precipitation estimates. There are important differences between the format and the properties of CML and SML raw data, as outlined hereafter.

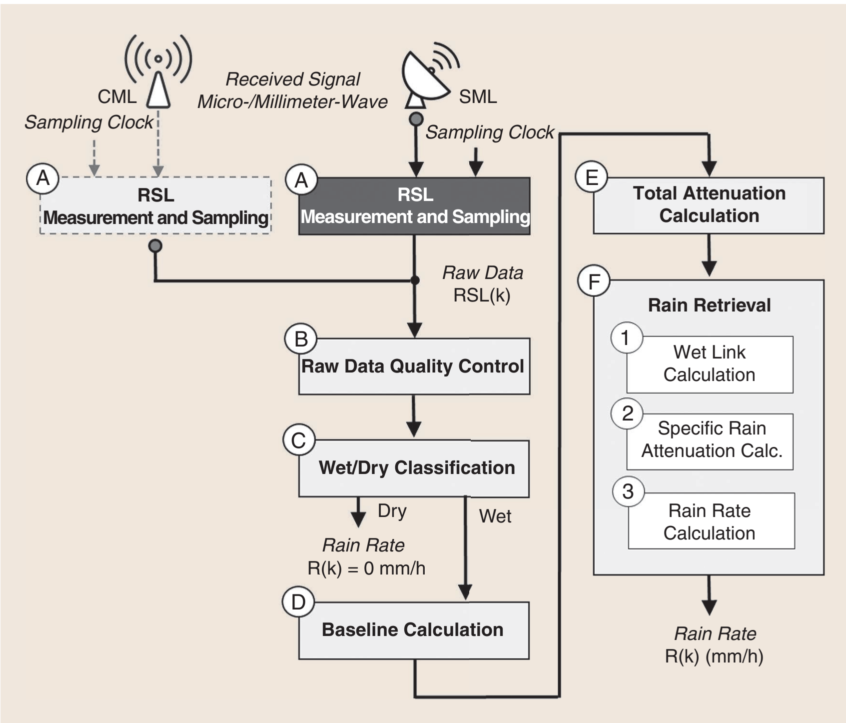

FIGURE 1. General flowchart for processing rainfall estimates from microwave link data (either CMLs or SMLs).

CMLs

The transmitters and the receivers of CMLs are part of the MNO infrastructure. RSL (and TSL) measurements are usually logged for link quality monitoring and maintenance purposes. They can be accessed only upon authorization of the MNO. Moreover, given the huge number of links operating in large terrestrial networks, routinely transmitting these data to a central server may pose issues. As a result, 1) the data available from CML networks are not optimized for precipitation estimation, and 2) the format and the sampling time of the RSL and TSL are parameters out of user control, being constrained by the data acquisition method chosen by each MNO. A MINMAX data format is adopted in several cases; that is, the minimum and maximum RSL and TSL values over a fixed observation window are logged. The size of the window is typically 15 min [53], [54]. In other cases, nearly instantaneous values collected every 1 min or at even shorter intervals are available [42].

In summary, in the case of CMLs, the tasks associated with the light-gray block in Figure 1 labeled "RSL Measurement and Sampling" are carried out by the MNO. The output sequence of RSL samples is made available by the MNO as "raw data" for precipitation studies.

SMLs

Satellite broadcast signals can be received anywhere within the satellite footprint and, unlike in the CML case, there are no data ownership issues. In particular, the RSL can be collected without any intellectual property or copyright infringement, any authorization from the broadcaster or the satellite operator, or any fee to be paid. Any commercial off-the-shelf (COTS) terminal for DTH satellite services carries out real-time RSL measurements for different purposes (e.g., installation, monitoring, maintenance, etc.). However, most COTS receivers do not support data logging. Therefore, RSL retrieval may entail some software or hardware modification of the device. This is not a straightforward task because of the lack of technical documentation from the manufacturers or intellectual property restrictions. Furthermore, some communication technology, either wired (Ethernet or asymmetric digital subscriber line) or wireless (Wi-Fi or 4G/5G networks), is necessary for transferring RSL data to the servers of a remote processing center.

One of the very few COTS satellite receivers allowing RSL retrieval is an innovative compact two-way device named SmartLNB [44], [55], which includes both an integrated DVB-S/S2 receiver and a transmitter for the return link (the ground-to-satellite link). The latter, besides user-generated contents for interactive TV services and local sensor data, also carries information about the status of the device, including high-rate readings (one or two samples per minute) of the SNR. These data are then uplinked to the satellite, which, in turn, relays them down to the processing center. This solution is simple and effective, but it requires a subscription fee for each SmartLNB and the availability of a return link. As an alternative to the use of COTS components only, a simple ad hoc custom board is proposed in [21]. It can be interfaced with the output of a commercial-grade universal low-noise block (LNB), i.e., the device that downconverts satellite signals from Ku band (RF) to L-band (IF) for DTH reception. This custom board samples the IF signals at short time intervals (e.g., 1 min) and processes them. The resulting RSL measurements are eventually transmitted to a remote processing server for real-time precipitation monitoring.

In summary, for SMLs, the RSL data can be obtained from direct measurements and subsequent processing of the microwave satellite signal by either a COTS receiver for DTH services or by an ad hoc terminal equipped with a custom board.

RAW DATA QUALITY CONTROL

Data quality control is fundamental when analyzing measurements collected from OSs. In fact, SML receivers often host commercial-grade equipment, whereas CML hardware can be neither controlled nor accessed by the user of the data. Moreover, in the CML case, even the metadata must be checked and regularly updated as mobile networks are continuously evolving, with links undergoing maintenance for a while, being upgraded, or sometimes dismissed and replaced by fiber optics.

The Raw Data Quality Control block of Figure 1 performs a number of basic tests over the time series of the RSL and TSL (if available). Standard tests on raw data include

- a search for missing data, that is, gaps in the time series. Short gaps (with respect to the dynamics of the observed process) can be filled by interpolation
- the identification of outliers (e.g., glitches or step-like variations in signal power)
- a cross-check of the data collected by different frequency channels of the same link or by nearby links.

A detailed step-by-step data quality control procedure is described in [56].

However, it is recommended to also carry out a data quality check on the outputs of each of the blocks following B in Figure 1, i.e., on the intermediate outputs as well as on the rainfall products. For instance, the RSL loss due to nonmeteorological factors, such as temperature effects on the receivers (described later in the section "Environmental Effects on the Sensor"), can be misclassified as light or moderate rain if samples are processed one by one. These patterns can be flagged once the events are identified (i.e., after block E or F), by comparing their features with those of rainfall. A quality control on rainfall products is performed in [19], where outliers are identified by cross-checking the rainfall estimates of each OS with those returned by the OSs in the neighborhood. In [57], opportunistic data gathered from CMLs as well as from personal weather stations are considered using a method developed for the latter. An additional quality control can be done on the statistics of the retrieved rainfall events considering monthly, yearly, or even longer periods of time as compared with the climatological data of the monitored area [58].

WET/DRY CLASSIFICATION

Labeling the RSL samples as "dry" or "wet" enables the detection of precipitation and the measurement of its duration. Moreover, it helps the subsequent steps of the processing chain in Figure 1, making it easier to estimate rain intensity. Wet/dry classification algorithms basically exploit the different features of the RSL wet samples with respect to the dry ones. For instance, RSL values are rather stable for CMLs in a dry atmosphere, which brings one to relatively simple wet/dry classification methods. By contrast, with SMLs, the RSL from GEO satellites, even in the absence of rain, may exhibit 24-h fluctuations because of the residual inclination of the satellite orbit with respect to the equatorial plane [26]. An operational GEO satellite has an inclination angle (typically lower than 0.1°), which produces SNR fluctuations up to ± 0.5 dB around the nominal level, when an 80-cm receiving parabolic dish is used (see the section "Environmental Effects on the Sensor" for more details). Hence, wet/dry classification methods for SMLs should take into account this impairment.

CMLs

Wet/dry classification can be done on an individual link basis by analyzing the time series of the RSL or of the signal attenuation. A simple method consists of calculating the standard deviation of the attenuation level on a sliding window of a suitable duration (e.g., 1 h). Fluctuations in the signal are detected when the standard deviation exceeds a threshold. The latter is usually defined by training the procedure over dry and wet periods of time previously identified by nearby rainfall sensors [59]. More sophisticated artificial intelligence (AI) methods have been used as well. For instance, the authors of [60] apply a technique based on convolutional neural networks (CNNs), while [61] adopts a type of recurrent neural network, namely long short-term memory (LSTM). Other methods exploit the spatial correlation of precipitation. In fact, during a rain event, the signals from neighboring CMLs are expected to exhibit similar fluctuations at close temporal intervals [48]. This property becomes more effective where dense CML networks are in place [22]. In [62], the authors propose a one-class classifier based on autoencoders, relying only on dry period data. This method achieves slightly better performance than an approach based on the RSL standard deviation. Wet/dry classification can be done indirectly as a result of the baseline level calculation [63] (see the next section). Other approaches make use of independent rainfall sensors, such as WRs [53], Earth observation satellites [64], or, again, a combination of the two [65].

SMLs

Because of orbit perturbations and drift, GEO satellites, as seen from Earth, do not appear perfectly still in the sky. As a result, the RSL undergoes slow fluctuations and variations over time scales of hours, which complicate the wet/dry classification task. In this respect, an approach based on two Kalman filters in parallel is effective, as shown in [44] and [66]. A slow tracker (ST) is configured to track only the slow variations due to orbit perturbations and drift, while a fast tracker (FT) detects faster RSL variations, such as the ones due to rain. By comparing ST and FT outputs, the start and the end of a rain event can be detected. Kalman filtering can be used as a general method to monitor the RSL and trigger rapid fluctuations due to an external disturbance.

AI methods used for wet/dry classification of SML data include artificial neural networks (ANNs), support vector machines (SVMs), or extremely randomized trees. They are trained using a set of statistical features extracted from the sequence of RSL samples [49], [67] or from a bandpass-filtered version of it [68]. AI methods based on observed time series (that do not require feature extraction) include a deep neural network approach based on an LSTM layer [69] or logistic regression based on measurements of the bit error rate. The work in [47] compares four AI algorithms: ANN, SVM, decision tree, and random forest. In [70] the same authors propose an online training procedure that includes a forgetting mechanism to increase the efficiency of the wet/dry classification task in embedded systems. In [71] the same authors employ AI to increase the performance of a statistical algorithm over a network of 26 SML links.

BASELINE CALCULATION

In principle, signal attenuation along the path can be derived from RSL and TSL measurements and link characteristics through the classical Friis propagation equation [72]. However, not all of the previous elements are known. For instance, TSL is not always stored into CML databases and is not available in the case of SMLs. Hence, rain attenuation is usually calculated from the difference (on a decibel scale) between the current RSL value and an RSL "baseline" value calculated in dry conditions (i.e., in the absence of rain).

Baseline estimation methods often rely on the wet/dry classification outcomes working out the baseline value as a statistical index of the RSL distribution over the dry periods before a rain event. For instance, [53] calculates the baseline as the median RSL value over the preceding 24 dry hours. This approach assumes that the baseline is constant during the entire rain event, which may be not the case, especially during long events. By contrast, dynamic techniques update the baseline level at every sample. For instance, [63] takes the minimum RSL over a suitable observation window (31 min with a 1-min raw data sampling), whereas [73] adopts a simple first-order linear low-pass filter. Calibration of the filter coefficient shows that the optimum baseline is the maximum between the previous and the current RSL sample. In principle, dynamic methods can work even without a preliminary wet/dry classification step.

RAIN ATTENUATION CALCULATION

The attenuation produced by rain is eventually evaluated at each sampling instant, based upon the current received RSL sample and the baseline level as follows.

CMLs

The RSL is typically the received power (P_R) in decibel-milliwatts. Rain attenuation (in decibels) at the generic kth sampling instant is

$$A(k)\ [\mathrm{dB}] = P_{\mathrm{BL}}(k) - P_R(k) \tag{1}$$

TOTAL ATTENUATION CALCULATION BASED ON SNR MEASUREMENTS IN SMLs

The kth sample of the SNR from an SML receiver in dry conditions can be written as [44]

$$\bar{\eta}(k) = \frac{\bar{E}_s(k)}{k_B\left[\frac{T_c}{L_{\text{atm}}} + T_m\left(1 - \frac{1}{L_{\text{atm}}}\right) + T_g + T_r\right]} \quad \text{(S1)}$$

where $\bar{E}_s(k)$ is the received energy in dry conditions, k_B is Boltzmann's constant; $L_{\text{atm}} = 10^{L_z^{(\text{dB})}/(10\sin\theta)}$ is the attenuation due to atmospheric gases, with $L_z^{(\text{dB})}$ the zenith atmospheric attenuation in decibels [91], and θ the satellite elevation above the horizon; T_c, T_m, T_g, and T_r are the noise temperatures of the microwave cosmic background, meteorological formations, ground, and receiver electronics, respectively. The latter temperature can be obtained from the noise figure $F^{(\text{dB})}$ provided (in decibels) by the manufacturer of the LNB, as $T_r = (10^{F^{(\text{dB})}/10} - 1)T_0$, where $T_0 = 290$ K is the customary room temperature.

The rain causes an extra attenuation $A(k)$ in the atmospheric medium with a twofold effect: 1) concerning the numerator, the signal energy is attenuated; 2) concerning the noise spectral density in the denominator, the contribution of the cold extraterrestrial noise T_c is attenuated, while that of the definitely hotter atmospheric noise T_m is increased, thus enhancing the overall noise PSD.

Accordingly, the kth sample of the SNR in wet conditions can be written as [44]

$$\eta(k) = \frac{\bar{E}_s(k)/A(k)}{k_B\left[\frac{T_c}{L_{\text{atm}}A(k)} + T_m\left(1 - \frac{1}{L_{\text{atm}}A(k)}\right) + T_g + T_r\right]}. \quad \text{(S2)}$$

Then, by combining (S1) and (S2), and with some manipulations [44], we eventually get the total rain attenuation as

$$A(k) = \frac{\bar{\eta}(k)}{\eta(k)}(1 - \xi) + \xi \quad \text{(S3)}$$

where we defined $\xi = (T_m - T_c)/[L_{\text{atm}}(T_m + T_g + T_r)]$.

Typical values of SNR parameters are listed in Table S1.

TABLE S1. TYPICAL VALUES OF SNR PARAMETERS IN SMLs.

PARAMETER	VALUE RANGE
$\bar{\eta}(k)$	8–11 dB
T_m	255–280 K
T_c	2.78 K
T_g	10–50 K
$F^{(\text{dB})}$	0.1–1 dB
T_r	6–75 K
$L_z^{(\text{dB})}$	$5\cdot10^{-2}$ dB @ 10 GHz
θ	>30°

where P_{BL} is the baseline power level in decibel-milliwatts. The preceding equation assumes that the TSL is constant throughout the observation period. However, an automatic transmit power control (ATPC) loop is usually in place, so that the TSL is increased when the RSL falls below a predefined threshold to ensure link availability, for instance, during heavy rain. If ATPC is active, additional information is required to estimate rain attenuation. In principle, the system should also collect the actual TSL time series (P_T), sampled at the same temporal resolution as the RSL. If the TSL is unavailable, data on ATPC magnitude and activation time should be provided, to implement RSL correction strategies [22]. As P_{BL} is usually estimated based on the RSL value in the dry atmosphere, a general expression for rain attenuation in decibels with varying TSL is

$$A(k)\ [\text{dB}] = P_{\text{BL}}(k) - P_R(k) + P_T(k) - P_T^0 \quad (2)$$

where P_T^0 is the nominal TSL, that is, the one in the dry atmosphere (in principle, P_T^0 is the TSL value at the time stamp when $P_{\text{BL}}(k)$ was calculated). Rain attenuation calculated by (2) may include, besides the contribution due to falling raindrops, other spurious components, discussed in the section "A Broad Classification of Disturbances Affecting OS Signals," which should be compensated in advance before converting attenuation into rainfall intensity.

SMLs

In the case where the RSL is a power level, a constant TSL is assumed. Since this value is unknown, the second member of (2) is reduced to the first two terms. If the RSL is instead expressed by the SNR, rain attenuation is given by the following [44]:

$$A(k) = \frac{\bar{\eta}(k)}{\eta(k)}(1 - \xi) + \xi \quad (3)$$

where $\eta(k)$ is the kth sample of the SNR during a wet interval, $\bar{\eta}(k)$ is the associated baseline level, and ξ is a quantity dependent on the components that contribute to the noise level measured at the receiver end. Details of the calculation of total attenuation from the SNR are discussed in "Total Attenuation Calculation Based on SNR Measurements in SMLs."

RAINFALL INTENSITY RETRIEVAL

Rainfall intensity can be retrieved from rain attenuation taking into account the geometry of the propagation path. The CML and SML scenarios in rain conditions are sketched in Figures 2 and 3 (as from [26] and [74]), respectively. Both figures show a case of stratiform rain, which is characterized by a well-defined layered structure. The vertical profile of precipitation is very important in the SML case, where the propagation path travels through the whole extent of the troposphere. In this respect, most of the SML rainfall retrieval algorithms assume stratiform precipitation since it is much simpler to model than convective rain. The accuracy of one of these algorithms in the presence of convective rain is assessed in [75] (see their Figure 8), using RG measurements as the ground truth. SMLs tend to underestimate rain intensity when convective precipitation is present. In fact, during the "mature" stage of precipitation, heavy rainfall causes large attenuation values, which may reduce the

RSL below the receiver sensitivity. On the other hand, rainfall estimates are rather accurate during the "developing" and the "dissipating" stages of precipitation [76].

Rainfall retrieval algorithms feature the processing steps detailed next, yielding an estimate of the rainfall intensity that represents an average value over the wet path, i.e., the rainy portion of length L of the propagation path.

1) *Wet link calculation*: Rain intensity may be nonuniform, either along the terrestrial path between the transmit and receiving antennas of a CML or along a slant SML path between the ground receiver and the top of the clouds. In the latter case, precipitation can also be affected by the "virga" phenomenon, i.e., a vertical variation of rainfall intensity with respect to ground level, due to a gradient of atmospheric parameters such as humidity, which can cause evaporation or sublimation of precipitation [77], [20]. As the actual spatial distribution of rain intensity is unknown, the wet path L is usually calculated assuming that the rainfall intensity is constant, both horizontally and vertically. That is, 1) for CML, rain is assumed uniform over the entire path, and 2) for SML, rain is uniform over the slant path from the ground station up to the rain height h_R. The latter is defined as the height above mean sea level where solid ice particles start melting into raindrops.
2) *Calculation of specific rain attenuation*: The estimated specific (per unit path length) rain attenuation γ over a wet path of length L at time k is obtained as
$$\gamma(k)\,[\mathrm{dB/km}] = A(k)\,[\mathrm{dB}]/L\,[\mathrm{km}]. \tag{4}$$
3) *Rain intensity calculation*: The rain intensity or rain rate $R(k)$ in millimeters/hour is usually estimated by inverting the following γ–R power-law relationship [78]:
$$\gamma(k)\,[\mathrm{dB/km}] = \alpha R(k)^{\varkappa} \tag{5}$$
yielding
$$R(k)\,[\mathrm{mm/h}] = \left(\frac{1}{\alpha\, L\,[\mathrm{km}]}\, A(k)\,[\mathrm{dB}]\right)^{1/\varkappa}. \tag{6}$$

The coefficients α and $\varkappa$ are tabulated by the International Telecommunication Union Radiocommunication Sector (ITU-R) [79] as a function of link frequency and polarization. However, even though ITU-R coefficients are largely used in engineering practice, they represent a coarse average, valid on a statistical basis. In principle, the relationship between R and γ also depends on the microphysics of rain. Therefore, some authors use values of α and $\varkappa$ coefficients calibrated with local disdrometers [80], [81].

The practical implementation of the rain retrieval algorithm has some important differences between CMLs and SMLs, as detailed in the following sections.

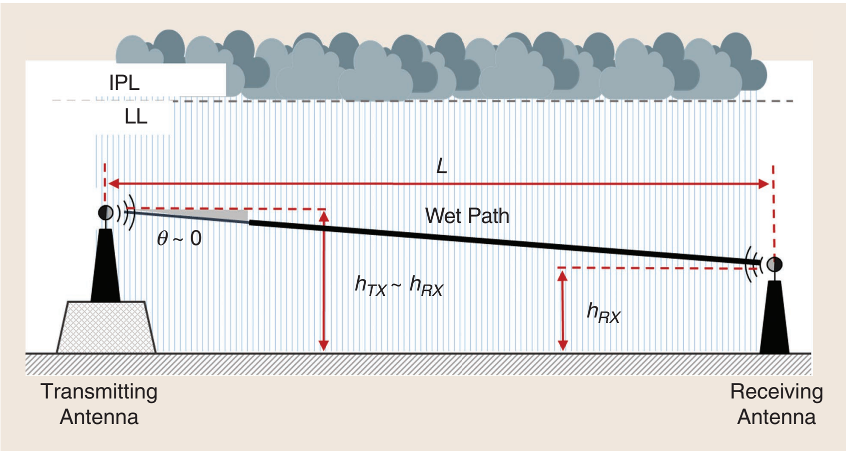

FIGURE 2. CML geometry in the presence of stratiform rain uniformly distributed along the path. IPL: ice particle layer; LL: liquid layer.

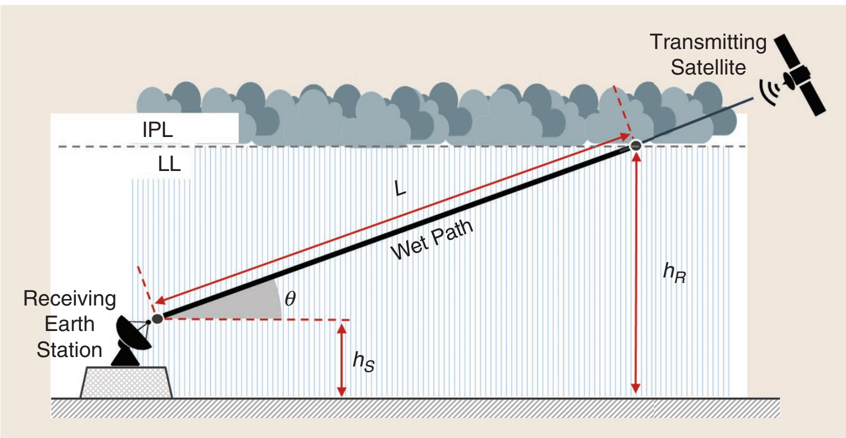

FIGURE 3. SML geometry in the presence of stratiform rain uniformly distributed along the path. A two-layer tropospheric model is adopted (as from [26] and [74]).

CMLs

The radio link of length L between two antennas of a mobile network is shown schematically in Figure 2. The link path is often nearly horizontal; i.e., the path inclination angle θ is close to 0°. Especially for links longer than a few kilometers, and depending on the local climate, it is possible, and maybe very likely, that the rainfall is not homogeneous along the path. However, since no information on the spatial distribution of precipitation along the link can be obtained from rain attenuation measurements, rainfall estimates from CMLs always represent average rain rate values along the entire link, rather than just along the wet path.

SMLs

The radio downlink between a satellite and a ground station for uniform stratiform precipitation and a simple two-layer tropospheric model are schematically shown in Figure 3. We assume a clear separation, at the rain height h_R, between two layers: 1) the upper layer, called the ice particle layer (IPL), mostly made of ice in the form of frozen dry particles, and 2) the lower layer, called the liquid layer (LL), which extends down to the ground and is characterized by the presence of liquid precipitation. The ground station is located at an altitude h_S above mean sea level and sees the satellite at an elevation angle θ above the horizon. The evaluation of the length of the wet path requires a knowledge of $h_{R,}$ which is dependent on the 0°C isotherm height h_0. Accurate estimates of h_R can be derived from real-time data, such as temperature at ground, observations from zenith-pointing WRs, or radiosonde measurements. However, this approach can be employed for a few measuring sites, usually for calibration and validation purposes; it is not practical if a widespread network of sensors is in place because of the complexity and cost. A valid alternative for obtaining near real-time estimates of h_R is to build from statistical data, mainly modeled on past observations. For instance, worldwide yearly average values for h_R can be derived from the corresponding h_0 values by the simple scaling law $h_R = h_0 + 0.36$ km [82]. A more accurate estimate of h_R can be gathered from short-term forecasts of h_0 produced by a mesoscale numerical weather prediction model, such as the Weather Research and Forecasting Model [83] or the High Resolution Model of the European Centre for Medium-Range Weather Forecasts [84]. This approach is a good compromise between accuracy and computational effort. Furthermore, the complexity of tropospheric phenomena leads to the adoption of more sophisticated propagation models. The rain height rarely coincides with the 0 °C isotherm because of the presence of the melting layer (ML), i.e., the intermediate layer between the IPL and the LL, where the ice particles falling from the clouds gradually melt into raindrops [44]. In this case, the three steps outlined previously are incorporated into an analytical formula that accounts for the geometry of the multiple tropospheric layers with the associated propagation features, taking the kth sample of total attenuation $A(k)$ as the input parameter and the associated rain rate $R(k)$ as the unknown [44].

A BROAD CLASSIFICATION OF DISTURBANCES AFFECTING OS SIGNALS

OS raw data are affected by several disturbances, which must be identified and, when possible, compensated for by the Raw Data Quality Control block of the processing chain in Figure 1, or at a later stage. Some of these effects have been investigated by using radar data to simulate CML path attenuation [85] or by elaborating from analytical models [86]. It is convenient to classify disturbances into three broad classes:

- effects due to electromagnetic wave propagation from the transmitter to the receiver (see the section "Propagation Effects")
- effects due to the interaction between link components (antennas, receiver, etc.) and the environment as well as to nonideal functioning, or malfunctioning, of the hardware itself (see the section "Environmental Effects on the Sensor")
- effects due to technical limitations of CMLs and SMLs when used as rainfall sensors. (see the section "Technical Limitations").

PROPAGATION EFFECTS

These effects can be further divided into those due to the interaction with atmospheric constituents (gases) or with the atmospheric particles sometimes present in the air, and those with objects interfering with the propagation path. The impact of these interactions on the received signal depends on many factors:

- characteristics of the signal, that is, the frequency, polarization, and size of the electromagnetic beam in the plane transverse to the propagation direction
- path length and path elevation angle
- characteristics of atmospheric particles (chemical composition, phase, shape, size, and number concentration)
- climatology of the site where the link is installed, including microclimatic effects
- height of the transmitting and receiving antennas above ground
- type of the surrounding environment (rural, suburban, urban, etc.).

The effects on the received signal are attenuation, i.e., loss of signal power measured at the receiver end with respect to propagation in free space, signal fluctuations around its mean value, and cross-polarization, i.e., partial transfer of signal power from the transmitted polarization to the orthogonal one. These impairments have been extensively studied, and many empirical and theoretical models are available [72], [87], [88], [89], [90].

Propagation effects are usually modeled as additive random processes. In this respect, the signal attenuation in (2) and (3) should be intended as an average over a time window short enough to track variations in rainfall intensity but long enough to average out signal fluctuations due to effects such as the continuous reshuffling of raindrops within the electromagnetic beam and the additive noise introduced by the receiver.

INTERACTION WITH ATMOSPHERIC COMPONENTS

In the frequency bands listed in Table 1, raindrops generally have the highest impact on the RSL. However, significant or at least nonnegligible effects can be produced by a plethora of other atmospheric components:

- gas absorption, in particular due to water vapor and oxygen (O_2) [91]
- clouds (for SMLs and for CMLs in mountainous environments), fog, and mist [92]

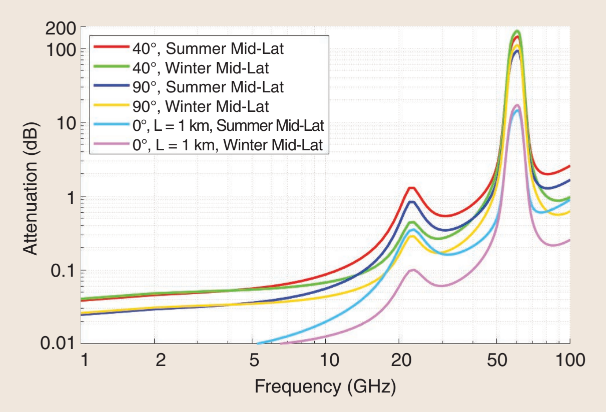

FIGURE 4. Gas attenuation as a function of frequency over terrestrial (0°) and slant paths with two different atmospheric conditions. Mid-Lat: mid-latitude.

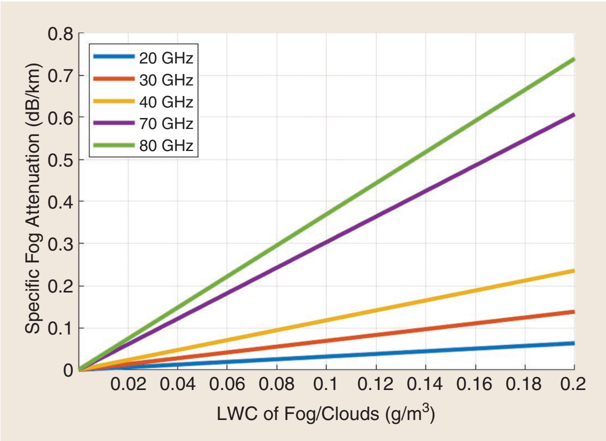

FIGURE 5. Fog/cloud attenuation per 1-km path length as a function of the LWC at five different frequencies.

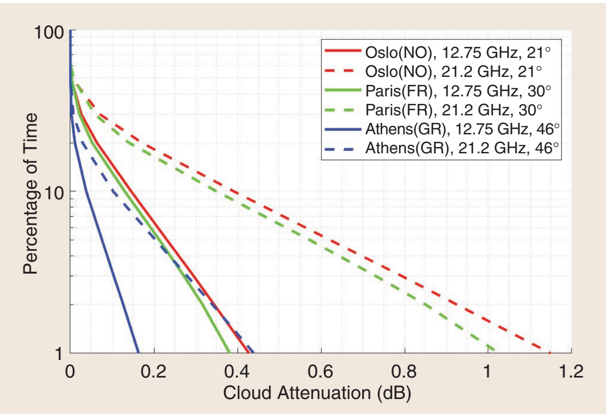

FIGURE 6. CCDF of cloud attenuation for SMLs in the Ku and Ka bands at three different locations.

- other types of hydrometeors (snow, hail, sleet, etc.) [93]
- dust and sand storms [94]
- ash and dust from volcanic emissions [95]
- tropospheric scintillation (SMLs only) [96], [97].

Gases are ever-present components, although the water vapor contribution is time variant even during rainfall because of humidity variations. Beyond 10 GHz, atmospheric gases may significantly contribute to path attenuation because of the presence of two major absorption peaks produced by water vapor and oxygen at 23 and 60 GHz, respectively. Figure 4 shows the frequency dependence of gas attenuation for three different path elevation angles and two different atmospheric conditions corresponding to summer and winter at midlatitude, according to ITU-R definitions [91], [98]. The curves at 40° and 90° (i.e., zenith) elevation are calculated across a path from sea level to a height of 10 km, while the curves for horizontal terrestrial paths are derived assuming, for convenience, a path length of 1 km. The average value of gas attenuation over a 40° satellite link at 20 GHz is around 0.6 dB, i.e., the same as for a 3-km terrestrial link. With CML path lengths of 5 km, which are not uncommon in mobile networks, especially outside city areas, the average gas attenuation is about 1 dB in summer (at 20 GHz), which corresponds to a rainfall intensity of 2 mm/h at the same frequency.

Fog and clouds are made by micrometric water droplets suspended in the air. The corresponding attenuation turns out to be proportional to the liquid water content (LWC) in the air, i.e., the mass of water particles in a unit volume of air. The attenuation across a 1-km path through fog/clouds is shown in Figure 5 at five different frequencies. The LWC of fog and clouds can range over orders of magnitude. For fog, an LWC value of 0.1 g/m^3 corresponds to dense radiation fog (visibility in the order of 100 m), while the LWC of heavy advection fog can be as high as 0.2 g/m^3. The LWC of clouds depends on the environment (i.e., maritime or continental) and on the type of cloud. Moreover, it is a function of the height above cloud base. The climatologic complementary cumulative distribution function (CCDF) of cloud attenuation (in decibels), derived through the ITU-R model [92], is shown in Figure 6 for satellite links at three different elevation angles in the Ku and Ka bands, respectively. The curves are terminated at 1% of time as it is assumed that rain attenuation dominates at lower percentages of time. Although gas and clouds produce maximum attenuation levels comparable to light rain, they may end in large overestimates of the accumulated rain, during long low-intensity events, if these components are not compensated for.

Melting ice particles and wet snow are able to produce large attenuation values over Earth–space links and even over terrestrial links, depending on the height of the link with respect to the rain height, which, in turn, depends on the geographic location and is time variant. [99] proposes a method to discriminate between rain and sleet (i.e., a mixture of rain and snow), from CML data only. ITU-R

[93] provides a correction factor for specific attenuation as a function of the difference between the height of the propagation path and the rain height. The contribution of melting ice particles is significant from the rain height down to 1,200 m below it, whereas attenuation due to ice particles above the rain height is negligible. Specific attenuation in the ML can be up to 3.5 times the one of rain at an equivalent liquid precipitation rate [100].

Wireless links operating in the microwave and millimeter-wave range of frequencies are severely affected by sand storms and dust storms. These events are frequent in the dry regions of the world (Central Asia, the Middle East, the southwestern United States, etc.). A comprehensive review of attenuation measurements and propagation models through sand storms and dust storms is provided in [94]. Attenuation increases as frequency increases and visibility decreases. Moreover, humidity has a huge impact on attenuation as it changes the dielectric constant of dust particles. Specific attenuation values in excess of 10 dB/km were measured at 21.3 GHz during severe dust storms in Khartoum, Sudan [101].

Volcanic eruptions are rare and sudden events that can have a significant impact on satellite communications, especially when large amounts of volcanic particles and gases are expelled in the atmosphere. An example is the eruption of the Eyjafjallajökull volcano in April 2010. The event triggered an ash cloud up to 9 km in height, causing significant attenuation at frequencies above 10 GHz [102].

Tropospheric scintillations are rapid amplitude fluctuations caused by small-scale irregularities in the refractive index of the air. They are not negligible for SMLs at frequencies above 10 GHz, and they increase with frequency. In the Ku band, fluctuations are within ±0.5 dB, and the period of scintillation fades varies from 1 to 10 s [96]. Therefore, these fluctuations are faster than signal variations during rain events.

INTERFERENCE EFFECTS

CMLs are usually mounted on tall masts, and they are carefully designed to prevent the electromagnetic wave from interacting with neighboring objects before reaching the receiver. It is usually considered that such interference is negligible if a region of space around the transmitter–receiver line-of-sight axis, known as the first Fresnel ellipsoid, is mostly free from obstacles. For instance, a 5-km link at 20 GHz has a loss within 0.5 dB because of partial clearance of the first Fresnel ellipsoid, if an area of a 7-m radius around the line-of-sight axis is free from obstacles at the midway point of the link. Possible sources of interference are the following:

- *Foliage*: It may induce only a partial clearance of the Fresnel ellipsoid, especially during spring and summer.
- *Multipath propagation*: Indirect signals may reach the receiver, for instance, after ground reflection.

ENVIRONMENTAL EFFECTS ON THE SENSOR

Inspection of CML and SML signals sometimes highlights peculiar patterns that are not related to propagation effects but rather to the interaction of the sensor with the environment.

CML AND SML COMMON DISTURBANCES

Reported sources of environmental disturbances that affect both types of sensors are as follows:

- *Rain, snow, and dew over the antenna*: The thin layer of water deposited by rainfall on the antenna (or on the antenna radome) can produce a significant extra attenuation. Wet antenna attenuation (WAA) adds up to rainfall attenuation while it is raining and is present even after the rain event, depending on the duration of the antenna drying process. If WAA is not accounted for, rainfall intensity may be heavily overestimated. Direct measurements of WAA require ad hoc setups, for instance, elevated sprinklers directing sprays of water to the antenna, which can simulate rain of different intensities [103]. Indirect measurements have been made by taking the difference between total link attenuation during rain and rainfall attenuation. The latter was calculated, for example, by electromagnetic theory from the drop size distribution (DSD) data collected by an array of disdrometers deployed along the path [104]. As measurements are expensive and, in principle, they should be carried out on each link in the network, WAA is usually estimated through empirical models. These models predict WAA from total attenuation (i.e., the difference between TSL and RSL), from rain attenuation, measured by the CML [103], [105], or from rainfall intensity, measured by either RGs [106] or by WRs [24], through simple analytical functions. The model parameters are calibrated using nearby RGs, or the parameter values derived in the original articles are assumed. The majority of models available for CML data predict an increase of WAA with rainfall intensity. For instance, the expressions proposed by [103] and [106] and derived from data at similar frequencies (27 and 32 GHz, respectively), predict WAA values slightly above 2.5 dB at 50 mm/h. These values are not negligible at all when compared with rain attenuation, that is, about 9 dB/km at 32 GHz [79]. Because of the several factors that affect WAA, including frequency, antenna setup, elevation angle, and weather conditions, it is recommended to calibrate CMLs by independent rainfall measurements.

  On the other hand, there is no evidence of any appreciable WAA effect in SML setups for DTH satellite TV reception featuring offset parabolic reflectors. This type of reflector exhibits a more vertical surface when compared to center-fed designs, which are rarely used for DTH reception. As a result, offset reflectors are less exposed to direct rain impact, thus reducing the effectivity of WAA.

  Concerning snow and ice effects, a significant overestimation of the precipitation was found in a CML-based countrywide study in Germany during the cold season, arguably due to the combined effect of melting snow along the path and ice and snow accumulation on the reflector surfaces [24]. Similarly, snow accumulation on the user terminal antennas at high latitudes has been found to cause severe attenuation on Ka-band satellite links for a significant fraction of time [107].

- *Thermal effects:* Thermal effects have an impact on RF circuits and antenna components, such as reflectors, as well as on mountings and masts. For CMLs, this results in slow and regular oscillations of the RSL with a clear daily pattern during warm sunny days. The magnitude of temperature often triggers this effect. Thermal effects may lead to labeling of dry slots as wet or to errors in the estimate of the baseline level, which, in turn, is used to derive rainfall intensity. An example is shown in Figure 7. SML systems relying on commercial-grade components for satellite TV reception are also prone to thermal effects. In particular, the LNB, which is mounted in the focus of the parabolic reflector, is exposed to sun rays and turns out to be the most vulnerable component to external temperatures. In this respect, the manufacturing quality and hence the cost of the device can make a significant difference in the sensitivity to thermal effects [108], as shown in Figure 8. Figure 8(a) presents the recorded RSL over a 24-h interval on a sunny and warm day (maximum temperature 28 °C) for both a conventional low-cost LNB (approximate cost €10) and a SmartLNB device (that costs approximately a few hundred euros), plotted as green and red lines, respectively. Figure 8(b) compares the fast-varying additive noise component affecting the two RSL records. As apparent, the cheaper LNB reveals a remarkable noise increase, strongly correlated with the external temperature (in blue), while the high-performance SmartLNB is almost insensitive to temperature variations.
- *Wind loading*: This may lead to misalignment, which, in turn, may cause an extra attenuation dependent on the inclination angle of the antenna pole with respect to the line-of-sight propagation direction. The inclination angle has a static and a dynamic component, the latter being due to the vibration frequency of the pole [109]. Both components are proportional to the square of wind velocity through a coefficient dependent on the type and length of the pole. Wind gusts can be responsible for misalignment and realignment events, that is, a sharp decrease or increase of the RSL.
- *Link malfunctioning*: Link malfunctioning produces several unwanted effects on the RSL, which can usually be detected by visual inspection. For CMLs, the most common anomalies are glitches, that is, sudden and short discontinuities in the signal (usually dips). An abnormal decrease of the RSL is sometimes observed, for instance, during heavy rain events due to water dropping into the antenna feed. Finally, the "no signal" status is observed for long periods during maintenance, for lack of power or link dismissal. Link failures may seldom be experienced by SMLs because the operator performs housekeeping maneuvers, power adjustment, TV channel reconfiguration, etc.

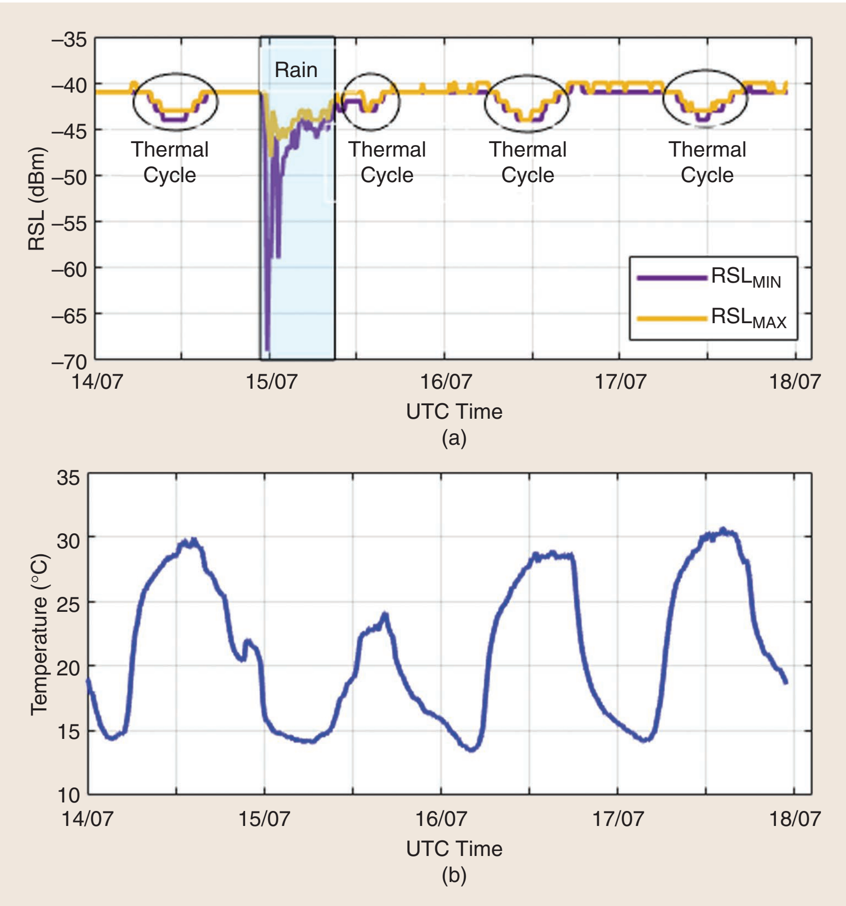

FIGURE 7. (a) Four-day record of RSL from a CML (41.082 GHz, 1,332 m), showing a rain event and thermal effects. (b) Corresponding temperature record highlighting the daily cycle. The RSL signal format is 15-min MINMAX. UTC: Coordinated Universal Time.

It is interesting to assess the percentage of OS raw data that are either missing or invalid. For brevity, we indicate such a case as NaN (Not a Number). A NaN occurs at discrete time k if $\mathrm{RSL}(k,i,n) = \mathrm{NaN}$ or $\mathrm{TSL}(k,i,n) = \mathrm{NaN}$, where i and n denote link and channel indices, respectively (the channel perspective). Alternatively, from a link perspective, a NaN occurs when $\mathrm{RSL}(k,i,n) = \mathrm{NaN}$ or $\mathrm{TSL}(k,i,n) = \mathrm{NaN}$ for every n; that is, if every link channel is NaN. Figure 9 shows the cumulative sum of the percentage of NaNs for two different CML datasets. Figure 9(a) shows the results for a set of 17 links in the area of Valmalenco, Lombardy, during a noncontinuous observation period of 1,056 h in 2019. Figure 9(b) shows NaNs on the raw data collected from a network of 151 CMLs in Emilia-Romagna (owned by a different MNO) during a continuous observation window of 4,344 h. Data are sampled every 1 min. In the Valmalenco dataset, the percentage of NaNs (raw data) is less than 4% for all links and is within 2% for 15 out of 17 links. In the Emilia-Romagna dataset, 142 out of 149 links (95% of the network) have less than 2% of NaNs. An analysis of data availability for the OpenMRG CML dataset [110], which includes 364 two-way links, that is, 728 channels or sublinks according to the authors' nomenclature, shows that 93% of the sublinks successfully collected more than 99% of the data.

SML PECULIAR DISTURBANCES

Because of the different link geometry, the following disturbances are peculiar to SMLs:

- *Orbit perturbations*: The orbit of any GEO satellite is slightly inclined with respect to the equatorial plane as a result of the gravitational effect induced by the Moon and the Sun. This implies that the satellite does not appear still in the sky when observed by a ground terminal. Instead, it moves around its nominal position along a figure 8-shaped path with a 24-h period [111], [112]. The corresponding angular variations, though small, are not negligible because of the narrow beam of the parabolic dish (Figure 10). In consequence, the RSL exhibits a 24-h periodic fluctuation. Further variations of the RSL are caused by the slow longitudinal drift of the satellite under the action of the gravitational forces caused by the longitudinal mass variations of Earth. To counteract these perturbations, the satellite position is periodically corrected by the satellite operator with "east-west" and "north-south" station-keeping maneuvers [113]. The combination of longitudinal drift and maneuvers renders the deterministic compensation of RSL fluctuations impractical.
- *Sun transit*: Twice a year, around the equinoxes, a GEO satellite is "blinded" by the apparent transit of the Sun behind the satellite. This phenomenon lasts about 20 min every day at the same time for a dozen days (Figure 10). During the sun transit, the Sun causes an increase of the noise temperature of the ground receiver [114], which may result in a degradation or a complete loss of the signal.
- *Adjustments of transponder transmit power*: Occasionally, the satellite operator changes the transponder gain settings because of customer requests or other operational needs. This adjustment is normally carried out in a very short time, and sometimes it may result in a reduction of the RSL (Figure 10).

TECHNICAL LIMITATIONS

When CMLs or SMLs are used as rainfall sensors, they have technical limitations, which bound their accuracy and

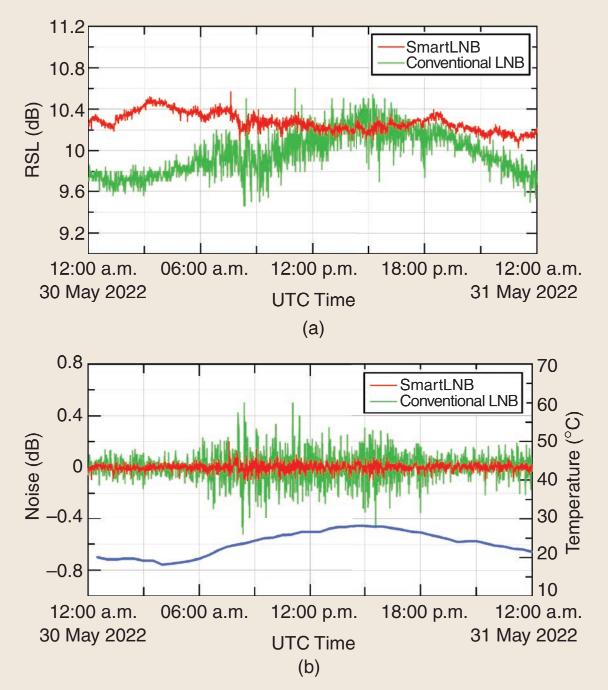

FIGURE 8. (a) 24-h RSL record collected by an SML equipped with a SmartLNB (red) and by one with a conventional LNB (green). (b) Corresponding fast noise component affecting the SmartLNB (red) and the conventional LNB (green) and daily temperature cycle (blue). The RSL signal is the instantaneous SNR sampled every 30 s.

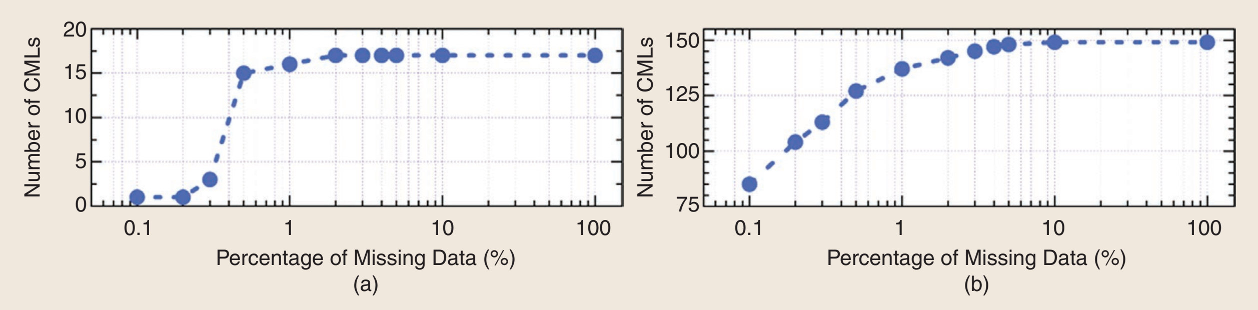

FIGURE 9. Cumulative sum of the percentage of missing data for two different CML datasets in Italy. (a) The Valmalenco dataset includes 17 CMLs, whereas (b) the Emilia-Romagna dataset has 149.

reliability, even in an ideal case in which the disturbances described in the sections "Propagation Effects" and "Environmental Effects on the Sensor" are fully compensated. Some major limitations are listed in the following sections.

TEMPORAL SAMPLING

CML raw data are often decimated before being stored and transmitted through the network to minimize bandwidth occupation as data are collected from thousands of devices. As a result, the temporal sampling of the available data ranges from less than 1 min, which is finer than the one of CSs (see Table 1), to 15 min, which may be too coarse to track the dynamics of rapidly changing convective cells. On the other hand, SML data sampling depends on the technical characteristics of the receiving devices. For instance, SmartLNBs sample the RSL at a fixed rate of one sample/second and return one averaged RSL value every 30 or 60 s (selectable by the user) [44]. Systems featuring ad hoc custom boards interfaced with conventional LNBs, like the one described in [43], provide raw data averaged over time scales similar to those of SmartLNBs. Other satellite receivers may have different (typically coarser) time resolutions. For instance, data from the two terminals of ViaSat's SurfBeam [115], which are used in the Konnect satellite platform for two-way broadband access in the Ka band [116], are collected and processed by the MNO service center every 15 min [117].

SPATIAL SAMPLING

Individual CMLs and SMLs produce path-integrated rainfall intensity estimates across horizontal and slant paths, respectively. In addition, the quantity actually measured by a link is the average rain attenuation across the path, rather than the rainfall intensity. These facts have two important consequences. First, as (6) is not linear, the retrieved rainfall intensity is not the arithmetic average across the path but instead an equivalent rainfall intensity. We note that if we substitute ITU-R coefficient values [79] into (5), then (6) turns out to be almost linear between 18.3 and 24.9 GHz, depending on the polarization and path elevation. Second, CMLs and SMLs are often modeled as point sensors located midway through the path. Some authors suggest to approximate the spatial distribution of rainfall across the path by two or more virtual RGs, deriving the rainfall intensity in each of the preceding points by an iterative method relying on nearby links [118].

The nonuniformity of the rain field along the wet segment has been tackled by several works, usually on a statistical basis, i.e., by applying a path-reduction factor to the rain attenuation value corresponding to a given probability level of the CCDF curve [93], [119], [120], [121]. For instance, [121] adopts a physical approach, modeling the spatial structure of the precipitation field by simple cylindrically shaped rain cell(s) filled with uniform rain, as shown in Figure 11. The path-reduction factor depends on link parameters (the length of the wet segment and the elevation angle) as well as on the features of the rain cells, in particular: 1) the diameter of a single rain cell, 2) the average length of the intersection between the ground projections of the slant path and of the individual rain cells, and 3) a calibration coefficient that considers the nonuniform distribution of rain inside a cell. The characteristic of the cells can be obtained, for instance, by a dataset of WR observations.

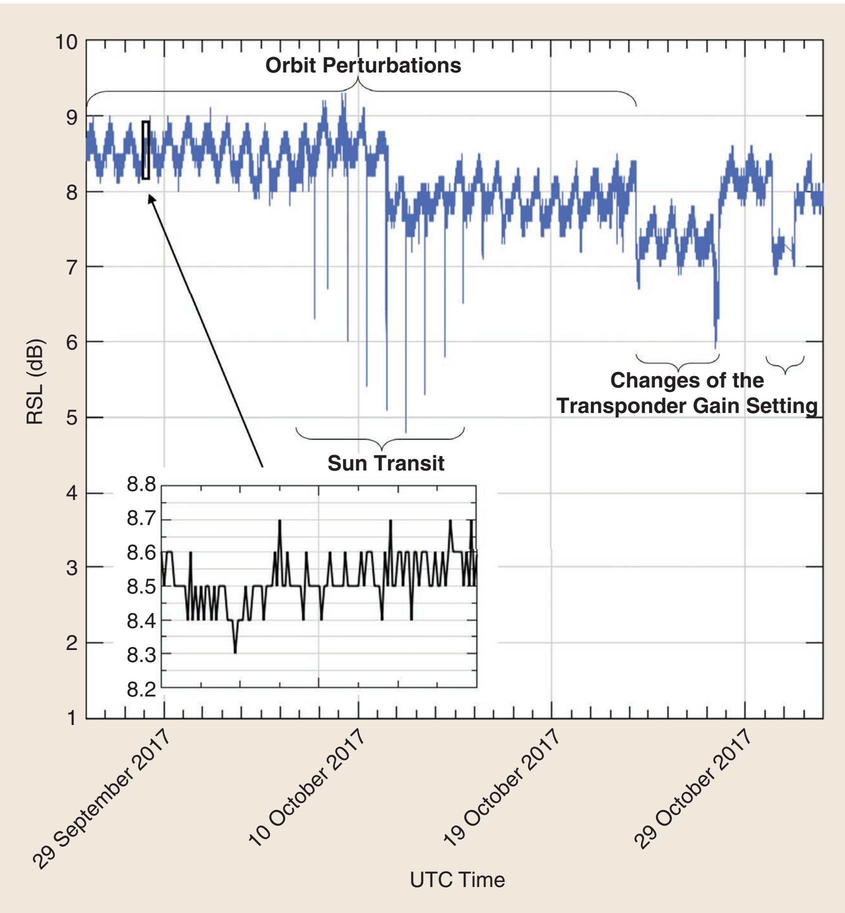

FIGURE 10. Record of the downlink RSL from a GEO satellite, showing several different impairments. The RSL signal format is the instantaneous E_s/N_0 at a 1-min sampling interval. (Courtesy from the authors of [26].)

RAINFALL FIELD RECONSTRUCTION

Retrieving 2D rainfall maps from 1D measurements has obvious limitations. The spatial reconstruction of the rainfall field from CML data is bounded by the density and the topology of the mesh of available links. It is usually done by interpolation techniques, such as inverse distance weighting or ordinary kridging [24], [122], [123], [124]. More sophisticated approaches include the adoption of rainfall advection models [125] or tomographic methods [126], [127]. To date, there are very few studies based on SML data. Some examples with synthetic rain are illustrated in [128] and [129]. The availability of many terminals of the EUROBIS satellite network [45], currently operated by MBI S.r.l. (Pisa, Italy), allowed the spatial reconstruction of the catastrophic flood event that devastated Germany in 2021; the methods used were interpolation [130] [131] and an innovative ensemble Kalman filter algorithm [132].

LINK CHARACTERISTICS

The different combinations of path length and operation frequency among the CMLs of a mobile network and between CMLs and SMLs lead to a different performance when they are used as rain intensity sensors, in terms of sensitivity, defined as the minimum detectable rainfall intensity and range of measurable rainfall intensities. Moreover, for CMLs, the usage of different antenna setups may lead to a different impact of WAA on different links, in principle, prompting for link calibration on an individual basis.

SIGNAL FORMAT

For CML data, the TSL and RSL are stored for purposes of link quality control. Hence, the data format is often not optimized for obtaining quantitative precipitation estimates, which results in

- a suboptimal sampling strategy
- inaccuracy due to signal quantization.

A MINMAX sampling strategy is sometimes implemented; that is, one measures the minimum and maximum RSLs within a given time window instead of using the average RSL value. Algorithms for estimating the average rainfall intensity from RSL extremes have been developed in [53] and [133]. Figure 12 shows the impact of the RSL quantization error on the sensitivity of CMLs and on their accuracy in estimating rainfall intensity. Four frequencies and two values of the quantization error are considered (0.1 and 1 dB), corresponding to lower and upper bounds for the datasets available in the open literature. Path length values are bounded to detect maximum rainfall intensity values corresponding to a maximum allowable rain attenuation of 50 dB. A 1-dB quantization error produces a substantial decrease of the minimum detectable rainfall intensity [Figure 12(a)] as links at frequencies below about 20 GHz are not sensitive to light rain (1 mm/h). Moreover, the accuracy is within 20% only if the rainfall intensity is above 10 mm/h and the frequency is in the Ku band or above [Figure 12(b)]. Hence, if CMLs will be used in the future for operational purposes, the raw data should have a quantization error in the order of 0.1 dB.

RSL-TO-RAINFALL INTENSITY CONVERSION

The conversion formula (5) with ITU-R coefficients is used in many studies based on OSs. However, it does not account for the microphysics of rain. The usage of $\gamma - R$ relationships obtained from local data is more representative of the climatology of the area of interest. As an example, Figure 13 shows (5) at the Ku and Ka bands (solid black lines) and the relationships obtained from data collected in Rome, Italy, by two different types of disdrometers: an OTT Parsivel sensor and a 2D Video Disdrometer (2DVD)—the latter being considered the benchmark for DSD measurements. While the OTT Parsivel and 2DVD are in good agreement, there are differences with the ITU-R relationship, particularly at the Ka band and at high rainfall intensities. Furthermore, using disdrometer

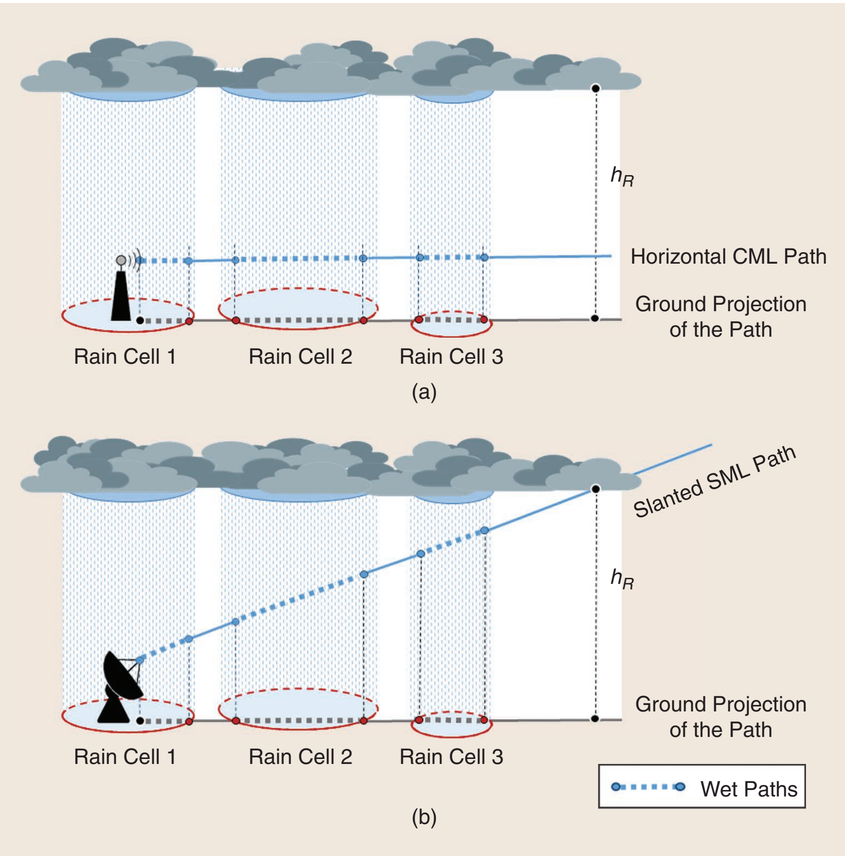

FIGURE 11. Precipitation along (a) a CML path and (b) an SML path, modeled by several cylindrically shaped rainfall cells with uniform rain intensity inside.

and WR data, the authors of [75] quantified errors in rainfall rate retrievals from SMLs produced by the ML geometry (height and thickness) and by the propagation models that derive attenuation from the precipitation rate in the LL and the ML, i.e., the power-law model (with the coefficients derived from disdrometer data) and the Dissanayake model [134], respectively. The results highlight a limited impact of the preceding factors [root-mean-square error (RMSE) $<$ 1 mm/h and normalized mean absolute error (NMAE) $<$ 20%]. These results need to be confirmed by data from other climatic locations and checked over a wider range of rainfall regimes.

DATA GATHERED FROM CMLs AND SMLs AS WELL AS OTHER OPPORTUNISTIC OR NON-PROFESSIONAL SENSORS BRING ADDED VALUE IF THEY ARE VALIDATED AGAINST CSs THROUGH RIGOROUS PROCEDURES.

DYNAMIC RANGE

Any SML receiver is characterized by a threshold RSL_{min}, which represents the lowest usable value of the RSL. Therefore, when the RSL falls below RSL_{min}, the device is no longer capable of measuring its actual value. This is called an outage, and it may occur during heavy precipitation. Hence, the rain rate corresponding to RSL_{min} represents the saturation value of the rain estimator, i.e., the maximum value that can be measured before the outage occurs. An as example, Figure 14 shows the performance of the SmartLNB system described in [44], wherein the data processed are transmitted by the satellite *Eutelsat 10A* in the Ku band (11.345 GHz) and collected by an 80-cm dish located in Pisa, Italy. The nominal SNR value in clear sky conditions is 11 dB, whereas the minimum SNR before outage is equal to –2 dB. The three curves convert the preceding 13-dB dynamic range into an interval of observable rain intensities for three different values of the 0 °C isotherm height, which represent a lower bound, an upper bound, and the yearly average in the measurement area, respectively. The dynamic range of CMLs is generally much higher than that of SMLs as CMLs are part of backhauling networks, which have very high availability requirements (typically 99.99% or even higher). In many cases, fade mitigation techniques, such as ATPC, are used to increase the dynamic range if heavy rain is present across the path. An analysis of gaps in CML data due to heavy rain is carried out in [58].

DATA TRANSFER

RSL data and other link quality indicators are usually logged by the network management systems provided by CML vendors. However, the format of these data is not optimized for weather monitoring. Alternatively, data can be polled through custom software based on protocols such as the Simple Network Management Protocol [135]. Transferring data from thousands of CMLs in a countrywide network to a cloud server for processing may be an issue, especially if real-time applications are targeted. Future systems may leverage edge computing for local processing of RSL data, reducing data transmission bottlenecks in large-scale OS networks.

MITIGATION OF DISTURBANCES

Assessing unwanted effects by automatic tests is not straightforward, and sometimes the task is done by visual inspection of signal patterns. In general, two classes of tests should be run.

1) The pattern of all events should be checked to avoid misclassifying unwanted effects as rain events.
2) When it is raining, one should quantify and separate unwanted effects from rainfall attenuation.

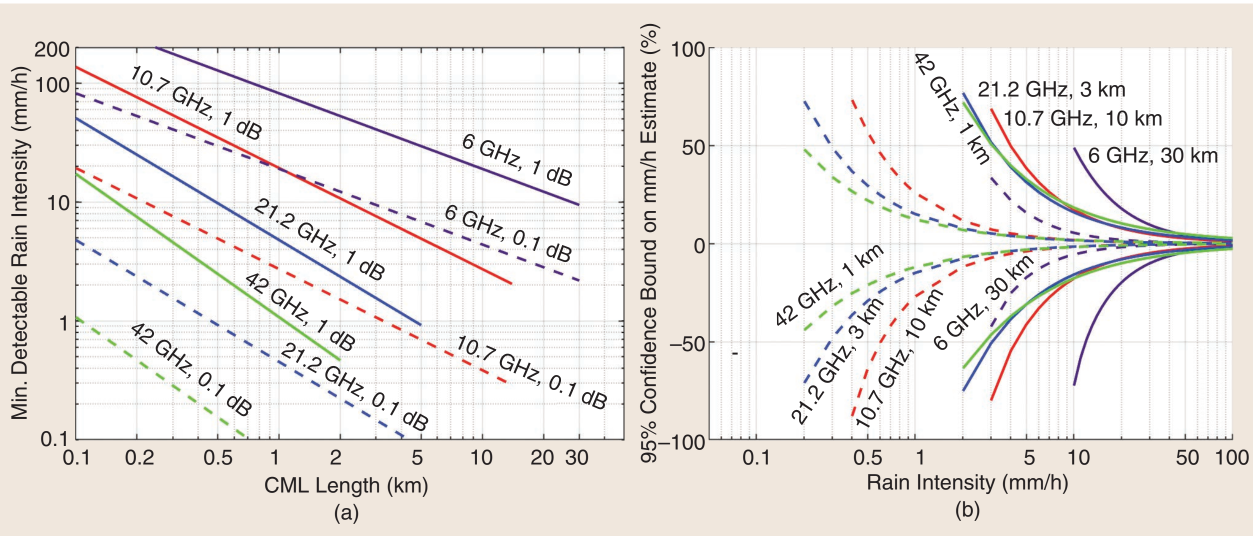

FIGURE 12. Effect of RSL quantization for two values of the quantization error: 1 dB (solid lines) and 0.1 dB (dashed lines). (a) Minimum detectable rainfall intensity against path length at four different frequencies. (b) Accuracy of rainfall intensity estimate against true rainfall intensity for different combinations of path length and frequency.

We note that, if dry/wet classification is done based on CML or SML data only, it may result in flagging dry periods as wet, for instance, during thermal events.

It is recommended to use concurrent weather data to help identify disturbances related to atmospheric and environmental conditions. Gas attenuation can be accurately predicted by the ITU-R model [91] from standard meteorological data (pressure, temperature, and relative humidity) that are collected from local weather stations. A procedure for correcting the baseline value according to predicted gas attenuation is described in [136]. Cloud attenuation detected by CMLs or by SML terminals at the Ku band is within 0.5 dB, while it is up to about 1 dB at the Ka band. As cloud events are not easily predictable from meteorological data, values of attenuation produced by clouds should be classified in advance as nonprecipitation events and discarded. Identifying events due to factors other than rain is basically a pattern recognition problem, and it is obviously more challenging for real-time applications than for analysis over historical data. Thermal effects are usually produced by temperature-induced variations in the amplifier gain at the received end. Sometimes, on-device compensation is carried out. As temperature triggers the process, data from weather stations may help in elaborating algorithms to correct or identify thermal events. However, RSL dips due to thermal effects, such as the ones in Figure 7, are rather easy to distinguish from rain as they exhibit a mild pattern correlated with the daily temperature cycle. A mere machine learning approach based on features such as the derivative of RSL and the difference between minimum and maximum RSL (in the case of MINMAX data) could be effective.

SML peculiar disturbances produced by GEO satellite orbit perturbations can be mitigated by averaging the baseline level over suitable time windows. Satellite diversity reception using a multi-LNB receiver setup is a possible strategy to counteract signal loss due to sun transit effects [137].

KPIs OF OS RAINFALL ESTIMATION ACCURACY

Data gathered from CMLs and SMLs as well as other opportunistic or non-professional sensors bring added value if they are validated against CSs through rigorous procedures. In this process, RG and WR data are usually taken as the ground truth. The quantities that are usually compared with the ground truth are rainfall occurrence (the output of wet/dry classification) and rainfall intensity averaged over a suitable observation period. Various metrics, often referred to as KPIs, are considered to compare the performance of OSs and CSs in detecting and quantifying rainfall. In the following, we first investigate a few important aspects that affect the calculation of KPIs, namely, the different spatial and temporal sampling of different rainfall sensors and the uneven characteristics of rainfall itself. Then, in the sections "KPIs for Wet/Dry Classification" and "KPIs for Rain Intensity Retrieval," we discuss the KPIs used for rainfall occurrence and rainfall intensity estimates, respectively, surveying the works on this topic.

The calculation of the KPIs requires one to associate each OS with one or several CSs. The different spatial sampling of the sensors prompts different association strategies. CMLs and SMLs provide path-averaged rainfall estimates over horizontal or slanted paths, whereas RGs collect data at a single point. WRs carry out volume scans at different elevation angles, which are subsequently combined and projected on the ground, resulting in rainfall products available over 2D spatial grids. CML and SML data can be compared with WR products by selecting the pixels of the radar grid that overlap the projected link path on the ground. The radar pixels are typically weighted by the fraction of the path that lies within each of them [24]. Note that the value of each (Cartesian) radar pixel (a dry/wet flag or a rainfall intensity

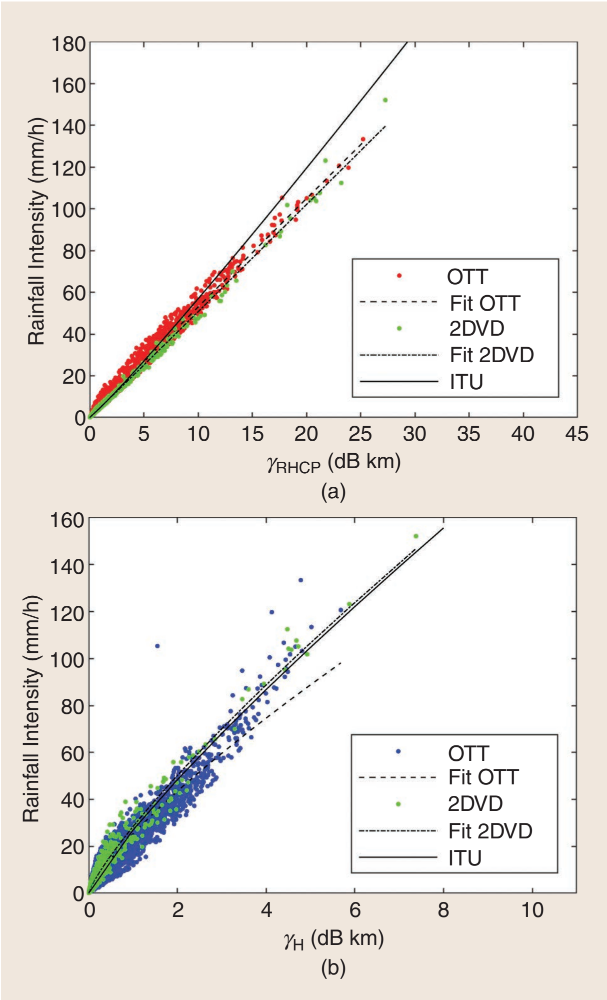

FIGURE 13. $\gamma - R$ scatterplots obtained from DSD data measured with two different disdrometers (OTT Parsivel and 2DVD HyMeX), in Rome, Italy. The specific attenuation γ is calculated at (a) the Ka band (29.74 GHz) and (b) the Ku band (11.387 GHz). The dashed and dash-dotted black lines in each graph are power-law best fits to the measured data, while the solid black line is the relationship provided by the ITU-R model [79]. 2DVD: 2D Video Disdrometer.

value) is a spatial average of measurements collected aloft by scanning volumes of space in spherical coordinates. On the other hand, RGs are usually associated with CMLs or SMLs by calculating the geometric distance between each RG and the nearest point, or the midpoint of the link path [123], [138]. An effective distance, which accounts for the path length and its relative position with respect to the RG, can be obtained by breaking the path into shorter segments and averaging the distances from the RG to the midpoint of each segment [81]. The minimum distance rule is the most obvious rationale used for the association. Alternatively, all of the RGs within a maximum distance $D_{\max}$ from the link are selected, and the ground truth is a linear combination of the RG measurements within $D_{\max}$ [139]. As a general rule, $D_{\max}$ should be lower than the spatial decorrelation distance of precipitation. For example, a study in the Emilia-Romagna region of Italy shows that KPIs are insensitive to the distance between CMLs and RGs as long as $D_{\max} < 3$ km [22]. This value is significantly shorter than the average decorrelation distance of precipitation in Italy [140], and it is also shorter than the length of the CMLs used in [22]. To conclude, associating CML or SML data to WR data is straightforward as the radar grid covers the entire link path. On the other hand, RG point measurements are representative of only a part of the path, depending on the relative position of the RG with respect to the link, and on the length of the path.

OS and CS data may have rather different temporal sampling spans, ranging from a few seconds to hourly or daily in the case of RG data. In general, it is observed that the agreement between OS data and the ground truth improves as the integration time increases (see the results shown in "KPIs for Rain Intensity Retrieval"). In fact, for comparisons between CMLs or SMLs and RGs (i.e., point sensors), increasing the integration time mitigates the effect of the spatial distribution of rain, even though it reduces the number of data points available to perform a solid statistical analysis. As a practical guideline, the use of a subdaily integration time scale, such as hourly intervals, can serve as an effective starting point. This approach can balance the need to capture detailed temporal variations with the requirement of maintaining a sufficiently large sample size for meaningful comparisons.

Rainfall is observed in a small fraction of time, usually lower than 10% in continental areas at midlatitude. In addition, the statistical distribution of rainfall intensity is skewed toward small values. Hence, it is important to rely on KPIs of wet/dry classification that account for data imbalance. Moreover, the calculation of KPIs of rain intensity estimates should be restricted to OS–CS pairs of samples with rain intensity values that exceed a minimum intensity threshold for both the OS estimate and the ground truth measurement. Otherwise, the calculation can be done in the cases where only the ground truth sample is above the threshold. Finally, when calculating rainfall intensity KPIs based on relative errors, small deviations from very low "true" values can lead to disproportionately high relative errors resulting from division by near-zero reference amounts.

KPIs FOR WET/DRY CLASSIFICATION

Wet/dry classification is a binary problem, in which rainy (wet) observations are labeled as positive samples, while nonrainy (dry) observations are labeled as negative. The labels are assigned by thresholding the rainfall intensity measured by CSs, taken as ground truth. In the case of RGs, the threshold is usually set based on the number of tips per unit time. Similarly, for WRs, a pixel is declared wet when the rainfall intensity (averaged over the pixel area) exceeds a certain threshold.

When comparing CMLs or SMLs with WRs, a link is flagged wet if the rainfall intensity value calculated from the weighted average of the overlapping radar pixels exceeds a threshold. For comparison with RGs, the link is given the same wet/dry label as the nearest RG or labeled according to the most probable wet/dry outcome obtained by combining nearby RGs. These tags are the true wet/dry assignments as they are based on ground truth data, which must be compared with the wet/dry tags estimated from CML or SML data. The latter are not determined by thresholding the rainfall intensity as wet/dry classification is a specific task that comes before rainfall intensity estimate in the processing chain of OS data (see Figure 1). Instead, statistical or AI algorithms are used to label wet/dry time intervals.

The KPIs used to assess wet/dry classification are two-class categorical indicators [141], [142]. We start by introducing the following terms:

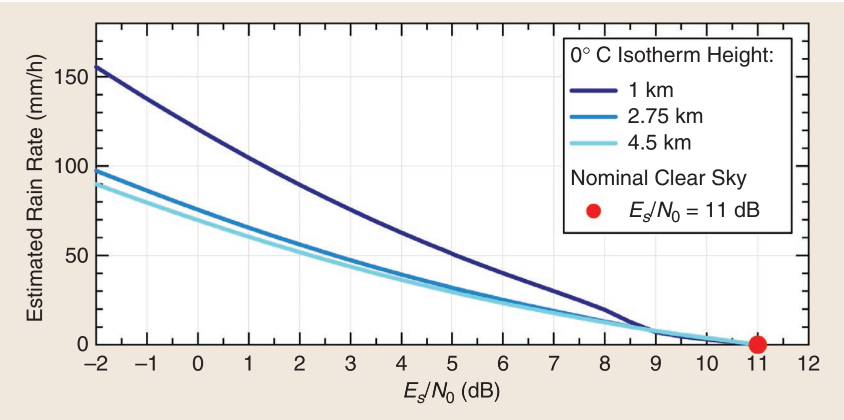

FIGURE 14. Dynamic range of an SML receiver expressed as estimated rain rate as a function of the measured SNR, i.e., E_S/N_0. If the SNR falls below –2 dB, the system is in outage. The three curves represent three different wet path lengths, corresponding to as many values of the 0 °C isotherm height.

- True positives (TP) are correctly classified wet samples.
- False negatives (FN) are wet samples incorrectly classified as dry.
- True negatives (TN) are correctly classified dry samples.
- False positives (FP) are dry samples incorrectly classified as wet.

By consequence,

- $n_{\mathrm{dry}} = \mathrm{TN} + \mathrm{FP}$ is the total number of dry observations.
- $n_{\mathrm{wet}} = \mathrm{TP} + \mathrm{FN}$ is the total number of wet observations.
- $n_{\mathrm{c,dry}} = \mathrm{TN} + \mathrm{FN}$ is the total number of observations classified as dry.
- $n_{\mathrm{c,wet}} = \mathrm{TP} + \mathrm{FP}$ is the total number of observations classified as wet.

KPIs are combinations of these quantities. A list of relevant KPIs is given in Table 2. The table is divided into three parts: the first one shows KPIs computed on the dry observations, the second has KPIs for the wet observations, and the last one has aggregated KPIs over wet and dry observations.

An important aspect to consider when calculating KPIs is the high data imbalance between wet and dry observations as the occurrence of dry periods is much higher than that of wet periods. Consequently, metrics, such as the accuracy score $(\mathrm{TP}+\mathrm{TN})/(n_{\mathrm{dry}}+n_{\mathrm{wet}})$ or the error score $(\mathrm{FP}+\mathrm{FN})/(n_{\mathrm{dry}}+n_{\mathrm{wet}})$, that give equal importance to wet and dry observations bias the evaluation of the performance. The aggregate KPIs proposed in Table 2, i.e., the harmonic mean (HM), mean detection error (MDE), and the Matthews correlation coefficient (MCC), account for this imbalance.

Table 3 shows the results of some key studies on wet/dry classification. SML studies are based on a few sensors as the SML ground receivers were usually deployed in the framework of ad hoc experiments. On the other hand, CML research builds from large datasets provided by MNOs and collected from networks of hundreds or thousands of operational links. Results based on smaller CML datasets and not reported in the table are provided in [143] and [62]. Other wet/dry classification works based on SMLs are presented in [47] and [68]. The table is structured over eight columns (from left to right): 1) bibliographical reference, 2) OS type (either CML or SML), 3) number of analyzed OS sensors, 4) sampling time of OS raw data, 5) length of the time window in which wet/dry labels are assigned (integration time), 6) overall observation period, 7) measured KPIs, and 8) notes on ground truth data, thresholds, and classification methods used. The KPIs in column 7 are calculated over the entire observation window for each sensor and represent median values over the population of OS sensors in the third column. As an exception, in [71] the KPIs were calculated on a daily basis, their median was subsequently computed over a 22-day observation period, and the result was eventually averaged over the 26 sensors.

AN IMPORTANT ASPECT TO CONSIDER WHEN CALCULATING KPIs IS THE HIGH DATA IMBALANCE BETWEEN WET AND DRY OBSERVATIONS AS THE OCCURRENCE OF DRY PERIODS IS MUCH HIGHER THAN THAT OF WET PERIODS.

It is not easy to compare the results collected from the preceding studies because of the many factors that may affect KPI values, which include 1) link characteristics, 2) data

TABLE 2. MOST SIGNIFICANT KPIs FOR THE WET/DRY CLASSIFICATION PROBLEM.

METRIC	FORMULA	DESCRIPTION
Specificity (Spe)	$\frac{\mathrm{TN}}{n_{\mathrm{dry}}}$	Indicates the classifier's ability to predict dry observations. It ranges between 0 (worst score) and 1 (best score).
False positive ratio	$\frac{\mathrm{FP}}{n_{\mathrm{dry}}}$	The complementary of Spe, indicating the classifier's inability to predict dry observations. It ranges between 0 (best score) and 1 (worst score).
False alarm ratio	$\frac{\mathrm{FP}}{n_{\mathrm{c,wet}}}$	The ratio of false alarms to predicted true samples. It ranges between 0 (best score) and 1 (worst score).
Recall (Rec)	$\frac{\mathrm{TP}}{n_{\mathrm{wet}}}$	Indicates the classifier's ability to predict wet observations. It is also referred to as *sensitivity* or *probability of detection*. It ranges between 0 (worst score) and 1 (best score).
False negative ratio	$\frac{\mathrm{FN}}{n_{\mathrm{wet}}}$	The complementary of the Rec metric, indicating the classifier inability to predict wet observations. It ranges between 0 (best score) and 1 (worst score).
Equitable threat score	$\frac{\mathrm{TP} - \frac{n_{\mathrm{wet}} \cdot n_{\mathrm{c,wet}}}{n_{\mathrm{dry}} + n_{\mathrm{wet}}}}{n_{\mathrm{wet}} + \mathrm{FP} - \frac{n_{\mathrm{wet}} \cdot n_{\mathrm{c,wet}}}{n_{\mathrm{dry}} + n_{\mathrm{wet}}}}$	Provides a better measure of a classifier's true skill to predict wet observations. It ranges from −1/3 to 1, where −1/3 is the worst score, 0 means no skill, and 1 is the best score.
HM	$\frac{2 \cdot \mathrm{Spe} \cdot \mathrm{Rec}}{\mathrm{Spe} + \mathrm{Rec}}$	The harmonic mean between the Spe and Rec metrics. It ranges between 0 (worst score) and 1 (best score).
MDE	$0.5 \cdot \left(\frac{\mathrm{FN}}{n_{\mathrm{wet}}} + \frac{\mathrm{FP}}{n_{\mathrm{dry}}}\right)$	The average of the missed wet and false wet rates. It ranges between 0 (best score) and 1 (worst score).
MCC	$\frac{\mathrm{TP} \cdot \mathrm{TN} - \mathrm{FP} \cdot \mathrm{FN}}{\sqrt{n_{\mathrm{wet}} \cdot n_{\mathrm{dry}} \cdot n_{\mathrm{c,dry}} \cdot n_{\mathrm{c,wet}}}}$	It summarizes the four values of the confusion matrix in a single measure. It ranges from −1 to +1, where −1 indicates perfect misclassification, +1 indicates perfect classification, and 0 indicates a performance not better than random guessing.

HM: harmonic mean; MDE: mean detection error; MCC: Matthews correlation coefficient.

quantization and sampling, 3) data processing, 4) integration time, 5) meteorological conditions and climate of the site where data were collected, 6) type of ground truth data, and 7) validation strategy. Finally, different sets of KPIs are used in different works. However, it is possible to compare KPI values obtained by different methods over the same dataset or to apply the same method over different datasets.

In [24] and [60], the data from 3,904 CMLs in Germany are compared with the RADOLAN-RW dataset from the German Weather Service (consisting of RG-adjusted radar products) by resampling the radar gridded data along individual CML paths. In particular, [60] shows that AI methods based on CNNs are better than statistical methods based on the standard deviation of the RSL, especially in rejecting FNs. Moreover, AI reaches an MCC value higher than that of statistical methods for at least 95% of CMLs. The KPIs in [22] are calculated comparing CML gridded rainfall data, obtained through the RAINLINK open software [51], against operational RG data gridded onto a 5 km × 5 km grid in the Emilia-Romagna region. The relatively low values of recall in [22] are probably due to the comparison being done on gridded products and to the coarse quantization (1 dB) of CML raw data. In fact, both contribute to increase the number of FNs. Aggregate indicators (HM) highlight that AI improves the performance over statistical methods even for SMLs [71]. We note that in the two studies featuring AI over CML and SML data, the recall is similar. On the other hand, the specificity is not comparable because of the different occurrence of dry samples in the two cases (i.e., a continuous six-month period in the CML case and only 22 rainy days in the SML case). Finally, [23] is the only study carried out on nearly instantaneously sampled data (i.e., a 1-min sampling interval).

KPIs FOR RAIN INTENSITY RETRIEVAL

Several different KPIs are used to assess the capability of CMLs or SMLs to estimate rainfall intensity [15], [21], [24], [56], [85], [145], [146], [147], [148]. KPIs can be categorized into two types: dimensional KPIs (those that have units) and dimensionless KPIs (those without units). The first category includes mean bias error (MBE), RMSE and bias-corrected RMSE, and mean absolute error (MAE). The second category includes relative bias (RB), NMAE, coefficient of variation (CV), normalized bias-corrected RMSE (NRMSE), root mean square of relative error (RMSE*r*), Pearson correlation coefficient (PCC), and Nash–Sutcliffe efficiency. Although both categories are important, the dimensionless KPIs are particularly advantageous as they enable fair performance comparison across datasets, regions, or in meta-analyses. In this respect, Table 4 presents a selected set of dimensionless KPIs together with the relative formulas and their meanings.

Table 5 summarizes the results of several relevant studies on the validation of rainfall intensity estimates obtained from CMLs and SMLs. This table has the same layout as Table 3. The last column reports, among others, the chosen threshold values for rainfall intensity, averaged over the integration time. Intensity values below the threshold are set to zero and discarded from KPI analysis. The first four rows in the table refer to validation studies of CML datasets in The Netherlands, which are also summarized in [147] (their Table A.1). CML data

TABLE 3. RELEVANT VALIDATION STUDIES OF WET/DRY CLASSIFICATION BY OSs.

REF.	OS TYPE	OS NUMBER	SAMPLING TIME	INTEGRATION TIME	OBSERVATION PERIOD	KPIs	NOTES
[22]	CML	308	15 min	1 h	57 days	FAR = .30 Rec = .54 ETS = .42	Ref.: gridded RG data Wet threshold: ref. > 0 mm Method: Statistical
[24]	CML	3,904	1 min	1 h	12 months	MDE = .27 MCC = .47	Ref.: RG-adjusted WR data Wet threshold: ref. > 0.1 mm Method: Statistical
[60]	CML	3,904	1 min	1 h	Six months	Spe ≈ .94 Rec = .62 MCC = .48	Ref.: RG-adjusted WR data Wet threshold: ref. > 0.1 mm Method: statistical
						Spe ≈ .97 Rec = .76 MCC = .69	Ref.: RG-adjusted WR data Wet threshold: ref. > 0.1 mm Method: AI
[71]	SML	26	1 min	5 min	22 rainy days	Spe ≈ .80 Rec > .80 HM ≈ .80	Ref.: WR data Wet threshold: ref. > 0.1 mm/h Method: AI
						Spe < .50 Rec > .95 HM ≈ .60	Ref.: WR data Wet threshold: ref. > 0.1 mm/h Method: statistical
[23]	SML	1	1 min	1 min	34 rain events in 12 months	Rec = .65 FAR = .15	Ref.: Disdrometer data Wet threshold: ref. > 0.1 mm/h Method: statistical

in the first three studies are sampled with a 15-min MINMAX strategy, while sampling is instantaneous in the last one (i.e., one sample every 15 min). A comparison of [147] with the version of the dataset in [146] validated with the same procedure highlights that MINMAX sampling performs much better than instantaneous sampling over the same 15-min window. Moreover, taking longer integration times improves KPIs. The results for the countrywide network in Germany in [24] are similar to the ones in [147] with a 1-h integration time, despite a much coarser sampling time in the former case. The work in [56] compares KPIs from two different CML networks across the German–Czech border. Several gaps and anomalous patterns in data, some of which are specific for one network only, were identified through extensive data quality control. Despite the different characteristics of the two networks, RB and PCC have similar values. Moreover, the authors show that the transboundary network provides composite rainfall maps able to reproduce the pattern of events as observed by WRs. Finally, the preceding work highlights large differences in the distribution of KPIs across CMLs. The metrics deteriorate for CMLs with a large value of the minimum detectable rain intensity because of the combined effect of link characteristics and data quantization, as also highlighted in the section "Technical Limitations" of this review. The analysis in [15] relies on only one available RG for validation. Nonetheless, it is an interesting case study relative to a region (Burkina Faso) where rainfall has different patterns than in Europe, and the CML network, located in the urban area of Ouagadougou, is made of relatively low-frequency links (10–13 GHz). The authors compare the RG daily accumulation with the one obtained by adding up the 5-min rainfall maps generated through spatial interpolation of CML data.

The SML validation works in [23], [75], and [149] are based on datasets collected by SmartLNB receivers of the same model in central Italy. The three sensors used in [149] are the same as in [23], and the observation periods are partially overlapped. In the former case, direct rainfall estimation is carried through AI from SNR data. As with dry/wet classification, KPIs of rainfall intensity highlight an edge of the AI approach over conventional methods based on the power-law expression (6). Two other recent studies based on AI techniques are presented in [150] and [151].

> **AS WITH DRY/WET CLASSIFICATION, KPIs OF RAINFALL INTENSITY HIGHLIGHT AN EDGE OF THE AI APPROACH OVER CONVENTIONAL METHODS**

CONCLUSIONS AND FUTURE TRENDS

We have surveyed the major technical challenges behind the usage of CMLs and SMLs as OSs for quantitative rainfall estimates. In both cases, the signature of precipitation, i.e., a decrease of the RSL, is contaminated by a number of unwanted disturbances. To mitigate these effects, the general processing chain of the RSL, highlighted in the flowchart of

TABLE 4. THE MOST SIGNIFICANT DIMENSIONLESS KPIs FOR RAIN INTENSITY RETRIEVAL.

METRIC	FORMULA	DESCRIPTION
RB	$\dfrac{1/N\sum_{i=1}^{N}(C_i-O_i)}{1/N\sum_{i=1}^{N}O_i}$	The average deviation between observed values (O_i), assumed as reference, and calculated (C_i) values, normalized to the mean of the observed values. N is the number of observations. It is often expressed in %. Values near 0 are good scores, negative values indicate underestimation, and positive values indicate overestimation.
NMAE	$\dfrac{1/N\sum_{i=1}^{N}\lvert C_i-O_i\rvert}{1/N\sum_{i=1}^{N}O_i}$	The mean absolute error divided by the mean of the observed values. It is often expressed in %. Lower NMAE values indicate better estimates.
CV	$\dfrac{\sqrt{1/(N-1)\sum_{i=1}^{N}(C_i-O_i)^2}}{1/N\sum_{i=1}^{N}O_i}$	The standard deviation of the differences between observed values (O_i), assumed as reference, and calculated (C_i) values, divided by the mean of the observed values. It takes nonnegative values. Values close to 0 indicate good scores.
NRMSE	$\dfrac{\sqrt{1/N\sum_{i=1}^{N}(C_i-O_i-MBE)^2}}{1/N\sum_{i=1}^{N}O_i}$	The normalized quadratic mean of the differences between observed (O_i) and calculated (C_i) values, where the MBE is subtracted, i.e., the numerator of RB. It is often expressed in %. It is dominated by the largest values because of the square operation.
RMSE$_r$	$\sqrt{\dfrac{1}{N}\sum_{i=1}^{N}\left(\dfrac{C_i-O_i}{O_i}\right)^2}$	The square root of the mean of the square of the relative errors $(C_i-O_i)/O_i$ between observed (O_i) and calculated (C_i) values. It is dominated by the largest values because of the square operation.
PCC	$\dfrac{\sum_{i=1}^{N}(O_i-\bar{O})(C_i-\bar{C})}{\sqrt{\sum_{i=1}^{N}(O_i-\bar{O})^2}\sqrt{\sum_{i=1}^{N}(C_i-\bar{C})^2}}$	It measures the linear relationship between observed (O_i) and calculated (O_i) values. $\bar{O}(\bar{C})$ represents the average of $O_i(C_i)$. It ranges from –1 to +1, where +1 indicates perfect linear correlation between the two datasets. However, a perfect linearity does not imply that the estimator is unbiased.

Figure 1, should also include specific algorithms (at least) for 1) identifying and discarding the RSL dips not produced by rain (e.g., due to thermal effects) and 2) quantifying the impact of WAA. The latter produces a significant extra signal loss during rainfall, which particularly affects CMLs. Moreover, CMLs and SMLs exhibit intrinsic limitations as rainfall sensors. CMLs are affected by the quantization of the RSL measurements, which limits their sensitivity and accuracy in detecting light rain. For example, a 1-mm/h intensity can be estimated with an accuracy within 20% only by the links operating above 10 GHz if the quantization error is as low as 0.1 dB. Furthermore, the maximum measurable rainfall intensity depends on the sensitivity of microwave receivers. The latter is the RSL threshold value below which the receivers are no longer capable of distinguishing the signal from system noise. In this respect,

TABLE 5. RELEVANT VALIDATION STUDIES OF RAIN INTENSITY RETRIEVAL BY OSs.

REF.	OS TYPE	OS NUMBER	SAMPLING TIME	INTEGRATION TIME	OBSERVATION WINDOW	KPIs	NOTES
[124]	CML	1,751	15 min	15 min	12 rainy days	RB = −13% CV = 1.44 PCC = .66	Ref.: RG-adjusted WR data Threshold: Ref. or CML > 0.1 mm
[146]	CML	3,383	15 min	15 min	2.5 years	RB = 1.6% CV = 5.58 PCC = .63	Ref.: RG-adjusted WR data Threshold: None Comparison on gridded data
[146][a]	CML	3,492	15 min	15 min	2.5 years	RB = 5.8% CV = 2.84 PCC = .52	Ref.: RG-adjusted WR data Threshold: Ref. or CML > 0 mm
[147]	CML	1,451	15 min	15 min	seven months	RB = 30% CV = 3.7 PCC = .30	Ref.: RG-adjusted WR data Threshold: Ref. or CML > 0 mm
				1 h		RB = 23% CV = 3.43 PCC = .52	
				One day		RB = 25% CV = 2.32 PCC = .63	
[24]	CML	3,904	1 min	1 h	12 months	RB = 30% CV = 3.03 PCC = .58	Ref.: RG-adjusted WR data Threshold: Ref. or CML > 0.1 mm
[56]	CML	1,167	1 min	1 h	One month	RB = −10% PCC = .93	Ref.: RG-adjusted WR data Threshold: Ref. or CML > 0.1 mm German network
		2,244				RB = −7% PCC = .86	Ref.: RG-adjusted WR data Threshold: Ref. or CML > 0.1 mm Czech network
[22]	CML	308	15 min	1 h	57 days	RB = −26% CV = .77 PCC = .68	Ref.: gridded RG data Threshold: Ref. or CML > 0 mm
[15]	CML	259	5 min	One day	Four months	RB ≈ −10% CV ≈ .55 PCC > .95	Ref.: RG data Threshold: not provided Only CMLs within 3 km from the RG
[21]	SML	37	1 min	10 min	16 rainy days	$RMSE_r$ = 1.6	Ref.: RG data Threshold: Ref. > 0.2 mm
[75]	SML	6	1 min	Event duration	12 months	NMAE = .55 RB = 19	Ref.: RG data Threshold: Ref. > 1.5 mm
[23]	SML	4	1 min	Event duration	12 months	NMAE = .50 RB = −18	Ref.: RG data Threshold: Ref. > 0.1 mm/h
[149]	SML	3	1 min	Event duration	24 months	NMAE = .11 PCC = .924	Ref.: RG data Threshold: Ref. > 1 mm

[a]Reprocessed data as discussed in [147].

CMLs, which provide wireless backhauling in the mobile networks and are based on professional-grade hardware, exhibit a better sensitivity to heavy rainfall than SML receivers, which are usually implemented by low-cost commercial devices.

The validation of rainfall estimates derived from CML or SML data requires a comparison with a ground truth, which is provided by conventional rainfall sensors. Rainfall occurrence (i.e., wet/dry classification), rainfall intensity, and rainfall accumulation over a given period are the primary variables analyzed. To this aim, it is necessary to define procedures for associating CML or SML measurements (i.e., a spatial average along a straight line) with RG and WR data (point measurements and 2D maps of rainfall, respectively), set thresholds on the minimum allowable rainfall intensity, and choose a set of suitable KPIs. Lists of relevant KPIs for assessing rainfall occurrence and rainfall intensity/accumulation are provided in Tables 2 and 4, respectively, whereas the results of major validation studies are summarized in Tables 3 and 5. The calculation of KPIs is influenced by factors such as the different spatial and temporal sampling between OS sensors and ground truth and the high variability of rainfall data. In this respect, temporal sampling adjustments, such as hourly or daily integration, should be used because they mitigate the previously discussed effects. Moreover, it emerges that AI techniques outperform conventional methods in detecting rain as well as in quantifying rainfall.

A clear trend in wireless communications is the exploitation of higher frequency bands because of congestion of the lower bands. In 2018, it was reported that most of the almost 5 million terrestrial wireless links active worldwide operate below 23 GHz [152]. Today, E-band technology is mature, and links in this bandwidth (71–86 GHz) have been operational for a few years. E-band links have already been studied for monitoring rainfall as well as water vapor [153]. Finally, even though the D-band (130–174.8 GHz) is still at the level of research, it represents an interesting challenge because of the availability of large amounts of the spectrum. Moreover, rain attenuation at the D-band is only marginally higher than at the E-band. In satellite communication systems, both broadcasting and broadband services are expected to shift toward the Ka band [154]. This, in turn, would open up interesting perspectives for opportunistic rainfall sensing as the increased rain attenuation [155] renders SML-based algorithms much more sensitive [117]. Satellite communications are also pointing toward the use of large and mega constellations of LEO satellites [156], [157]. Obviously, rain attenuation also has an impact on the performance of the downlinks of LEO satellite networks, especially those operating in the Ka band [158]. An analysis of rain effects on LEO ground stations is presented in [159] for some European locations. In a future perspective, LEO links could help produce 3D tomographic maps of the atmosphere [160].

Future developments in rainfall monitoring include the implementation of synergic data fusion-based networks featuring OSs. For instance, [144] proposes a reconstruction of precipitation fields through a stochastic approach from RG and CML estimates. [132] presents a framework for dynamically generating gridded rainfall fields through an ensemble Kalman filter approach, in which data assimilation techniques are used to merge the information from SML observations with forecasts produced by a rainfall advection model. The technique has been validated in synthetic rain scenarios. In [19], the authors demonstrate the merging of data from WR, personal weather stations, and CMLs into an integrated rainfall product. Finally, in [20], it is shown that a set of gap-filling SML terminals significantly improves the accuracy of 2D rain cell reconstruction gathered from a CML network in a synthetic rain environment.

FUTURE DEVELOPMENTS IN RAINFALL MONITORING INCLUDE THE IMPLEMENTATION OF SYNERGIC DATA FUSION-BASED NETWORKS FEATURING OSs.

ACKNOWLEDGMENT

This work was supported by the following projects: SCORE, funded by the European Commission's Horizon 2020 research and innovation program under Grant agreement 101003534; Space It Up, funded by ASI and the Ministry of University and Research (MUR) – Contract 2024-5-E.0 - CUP I53D24000060005; the RETURN project (Multirisk science for resilient communities under a changing climate) with Extended Partnership, which received funding from the European Union NextGeneration EU, National Recovery and Resilience Plan, Mission 4,525 Component 2, Investment 1.3—D.D. 1243 2/8/2022, PE0000005; FoReLab (Departments of Excellence), funded by MUR; the CLIMAXPO (LIFE21-IPC-IT-LIFE CLIMAX PO-101069928) and MODMET agreement (years 2024/2025) between the Italian National Civil Department and Arpae-SIMC; the CORAL project, funded under the first Open Call of the HORIZON-JU-SNS-2022-STREAM-D FIDAL project (Grant No. 101096146); and the European Cooperation in Science and Technology (COST) Action CA20136 OPENSENSE, funded by COST.

AUTHOR INFORMATION

Roberto Nebuloni (roberto.nebuloni@cnr.it) is a researcher at the Institute of Electronics, Computer and Telecommunication Engineering of the National Research Council (CNR-IEIIT), 20133 Milan, Italy. His early work was dedicated to the experimental activity at the CNR WR facility in Spino d'Adda, Italy, and aimed at rainfall modeling for radio propagation applications and environmental monitoring. His core research is on the characterization of millimeter-wave and optical wave propagation for applications such as adaptive Satcom systems, smart radio environments, and precipitation monitoring. He is a

board member of the Working Group on Propagation of the European Association on Antennas and Propagation. He has authored and coauthored more than 90 papers in international journals and conferences and three chapters in scientific books.

Filippo Giannetti (filippo.giannetti@unipi.it) is a professor of telecommunications in the Department of Information Engineering of the University of Pisa, 56122 Pisa, Italy. He worked on several international projects (the European Union's FP7 and the European Space Agency's H2020) and authored more than 200 journal and conference papers. He is a co-inventor of several patents, including an innovative technique for rainfall estimation based on opportunistic measurements of satellite signal strength. His main research interests concern digital signal processing, wireless communications, satellite systems, radio propagation, and rainfall measurement.

Fabiola Sapienza (fabiola.sapienza@ing.unipi.it) received her master's degree in telecommunications en gineering from the University of Pisa, Italy, in July 2020. Since December 2020, she has been a research fellow with the Department of Information Engineering at the University of Pisa, 56122 Pisa, Italy, with experience in the analysis and processing of satellite signals. As part of the INSIDERAIN project, she has been involved in the calibration and optimization of a rainfall estimation algorithm based on opportunistic measurements from satellite microwave links data. She is actively involved in the SCORE and Space It Up projects, continuing her research on satellite technology applications for environmental monitoring and data analysis.

Vincenzo Lottici (vincenzo.lottici@unipi.it) is a professor of communication systems in the Department of Information Engineering of the University of Pisa, 56122 Pisa, Italy. He participated in several international research projects (for the European Space Agency, FP7 and H2020) and standardization activities (for ETSI) and collaborated in joint research works with the Delft University of Technology (The Netherlands), George Mason University (Fairfax, VA, USA), the University of Ghent (Belgium), and Université Catholique de Louvain (Belgium). He authored more than 150 international publications and is a member of the editorial board of *EURASIP Journal on Wireless Communications and Networking*. His research interests include the broad area of signal processing for terrestrial and satellite communications, with an emphasis on synchronization, dynamic resource allocation, waveform adaptation, cooperative and cognitive wireless networks, ultrawideband communications, and compressive sensing techniques.

Elisa Adirosi (elisa.adirosi@cnr.it) received her master's degree in environmental engineering and her Ph.D. degree in environmental and hydraulic engineering from the Sapienza University of Rome, Rome, Italy, in 2009 and 2015, respectively. She has been a visiting scientist at Goddard Space Flight Center, NASA, Greenbelt, MD, USA, and is a researcher with the Institute of Atmospheric Sciences and Climate of the National Research Council, 00133 Rome, Italy. She develops innovative mathematical methods to analyze disdrometer data and investigates the characteristics of simulated and observed drop size distributions to improve precipitation retrieval from remote sensing measurements. She has been involved in the national NEFOCAST and INSIDERAIN projects and is now involved in an international SCORE project on rainfall retrieval from satellite microwave links data.

Giacomo Roversi (g.roversi@isac.cnr.it) is a Ph.D. student in the National Doctoral Programme in Polar Sciences at Ca' Foscari University, 30172 Venice, Italy, and he is based in Rome at the Institute of Atmospheric Sciences and Climate of the National Research Council of Italy. His research focuses on precipitation and cloud microphysics remote sensing from the ground, from satellites, and from opportunistic sensors. In collaboration with MEEO S.r.l. and Arpae Emilia-Romagna, from 2016 to 2020, he developed the first commercial microwave links rainfall product at regional scale in Italy.

Elia Covi (ecovi@arpae.it) received his master's degree in physics of the earth system from the University of Bologna, Italy, in December 2021. Since April 2022 he has been working at the Hydro-Meteo-Climate Structure of Arpae Emilia-Romagna, 40138 Bologna, Italy, where he is involved in activities related to the use of radar and commercial microwave links (CML) data over the region. Within the MODMET and CLIMAXPO projects, he works on operational applications of CML and on the combined use of opportunistic and conventional sensors.

Christian Gianoglio (christian.gianoglio@unige.it) received his master's degree in electronic engineering and his Ph.D. degree in electrical engineering from the University of Genoa, Genoa, Italy, in 2015 and 2018, respectively. He is a research fellow with the Department of Naval, Electrical, Electronic, and Telecommunications Engineering, University of Genoa, 16126 Genoa, Italy. His research interests include machine learning for resource-constrained devices and real-time applications, signal processing and machine learning for tactile sensing systems and rainfall classification, and pattern recognition for quality assessment of insulation systems in electrical apparatuses. He is a Member of IEEE.

Matteo Colli (m.colli@artys.it) received his M.S. degree in water and soil defense engineering and his Ph.D. degree in fluid dynamics and environmental engineering processes from the University of Genoa, Genoa, Italy, in 2010 and 2014, respectively. From 2014 to 2017, he was a research assistant with the Department of Civil, Chemical and Environmental Engineering, University of Genoa. From 2017 to 2019, he was a research assistant with the Department of Electrical, Electronics and Telecommunication Engineering and Naval Architecture, also at the University of Genoa. Since 2019, he has been the CTO of Artys, a business unit of Darts Engineering, 16121 Genoa, Italy.

Carlo De Michele (carlo.demichele@polimi.it) has been a professor of hydrology and water resources engineering in the Department of Civil and Environmental Engineering at Politecnico di Milano, 20133 Milan, Italy, since June 2019. He is an active member of several prestigious scientific organizations, including the International Association of Hydrological Sciences, the European Geosciences Union, and the American Geophysical Union. His research interests are broad and impactful, encompassing statistics, stochastic and multivariate modeling of hydrologic extremes, and climate and environmental variability effects. He has also made significant contributions to understanding precipitation dynamics and hydrological extremes in univariate and multivariate settings, including compound climate-related extremes. His publications include more than 160 international publications, eight book chapters, and two books published by Springer.

REFERENCES

[1] J. A. Smith, M. L. Baeck, A. J. Miller, and E. L. Claggett, "Rainfall frequency analysis based on long-term high-resolution radar rainfall fields: Spatial heterogeneities and temporal nonstationarities," *Water Resour. Res.*, vol. 60, no. 3, pp. 1–21, 2024, doi: 10.1029/2023WR035640.

[2] C. D. Ahrens and R. Henson, *Essentials of Meteorology: An Invitation to the Atmosphere*, 8th ed. Boston, MA, USA: Cengage Learning, 2018.

[3] A. Falkovich, E. Kalnay, S. Lord, and M. B. Mathur, "A new method of observed rainfall assimilation in forecast models," *J. Appl. Meteorol. Climatol.*, vol. 39, no. 8, pp. 1282–1298, 2000, doi: 10.1175/1520-0450(2000)039<1282:ANMOOR>2.0.CO;2.

[4] M. Borga, "Accuracy of radar rainfall estimates for streamflow simulation," *J. Hydrol.*, vol. 267, nos. 1–2, pp. 26–39, 2002, doi: 10.1016/S0022-1694(02)00137-3.

[5] S. Eggimann et al., "The potential of knowing more: A review of data-driven urban water management," *Environ. Sci. Technol.*, vol. 51, no. 5, pp. 2538–2553, 2017, doi: 10.1021/acs.est.6b04267.

[6] D. Dunkerley, "Recording rainfall intensity: Has an optimum method been found?" *Water*, vol. 15, no. 19, 2023, Art. no. 3383, doi: 10.3390/w15193383.

[7] N. Nanding and M. A. Rico-Ramirez, "Precipitation measurement with weather radars," in *The Handbook of Environmental Chemistry*, A. Scozzari, S. Mounce, D. Han, F. Soldovieri, and D. Solomatine, Eds., Cham, Switzerland: Springer-Verlag, 2019, pp. 235–258.

[8] A. Battaglia et al., "Spaceborne cloud and precipitation radars: Status, challenges, and ways forward," *Rev. Geophys.*, vol. 58, no. 3, pp. 1–59, 2020, doi: 10.1029/2019RG000686.

[9] Y. Hong et al., *Remote Sensing Precipitation: Sensors, Retrievals, Validations, and Applications*. Berlin, Germany: Springer-Verlag, 2018.

[10] E. Adirosi et al., "Database of the Italian disdrometer network," *Earth Syst. Sci. Data*, vol. 15, no. 6, pp. 2417–2429, 2023, doi: 10.5194/essd-15-2417-2023.

[11] A. Berne, G. Delrieu, J.-D. Creutin, and C. Obled, "Temporal and spatial resolution of rainfall measurements required for urban hydrology," *J. Hydrol.*, vol. 299, nos. 3–4, pp. 166–179, 2004, doi: 10.1016/S0022-1694(04)00363-4.

[12] C. Kidd et al., "So, how much of the earth's surface is covered by rain gauges?" *Bull. Amer. Meterol. Soc.*, vol. 98, no. 1, pp. 69–78, 2017, doi: 10.1175/BAMS-D-14-00283.1.

[13] J. Bliefernicht, S. Salack, M. Waongo, T. Annor, P. Laux, and H. Kunstmann, "Towards a historical precipitation database for West Africa: Overview, quality control and harmonization," *Int. J. Climatol.*, vol. 42, no. 7, pp. 4001–4023, 2022, doi: 10.1002/joc.7467.

[14] F. Tigrine, L. Barthès, and C. Mallet, "Opportunistic rainfall measurements from dual channel KU-band receiver," in *Proc. IEEE Int. Conf. Acoust., Speech, Signal Process. Workshops (ICASSPW)*, Rhodes Island, Greece, 2023, pp. 1–5, doi: 10.1109/ICASSPW59220.2023.10193748.

[15] M. Djibo, C. Chwala, M. Graf, J. Polz, H. Kunstmann, and F. Zougmoré, "High-resolution rainfall maps from commercial microwave links for a data-scarce region in West Africa," *J. Hydrometeorol.*, vol. 24, no. 10, pp. 1847–1861, 2023, doi: 10.1175/JHM-D-23-0015.1.

[16] K. K. Kumah, B. H. Maathuis, J. Hoedjes, and Z. Su, "Near real-time estimation of high spatiotemporal resolution rainfall from cloud top properties of the MSG satellite and commercial microwave link rainfall intensities," *Atmos. Res.*, vol. 279, Dec. 2022, Art. no. 106357, doi: 10.1016/j.atmosres.2022.106357.

[17] A. Overeem et al., "Tropical rainfall monitoring with commercial microwave links in Sri Lanka," *Environ. Res. Lett.*, vol. 16, no. 7, 2021, Art. no. 074058, doi: 10.1088/1748-9326/ac0fa6.

[18] M. Graf et al., "Rainfall estimates from opportunistic sensors in Germany across spatio-temporal scales," *J. Hydrol.: Reg. Stud.*, vol. 37, Oct. 2021, Art. no. 100883, doi: 10.1016/j.ejrh.2021.100883.

[19] J. Nielsen et al., "Merging weather radar data and opportunistic rainfall sensor data to enhance rainfall estimates," *Atmos. Res.*, vol. 300, Apr. 2024, Art. no. 107228, doi: 10.1016/j.atmosres.2024.107228.

[20] F. Saggese, V. Lottici, and F. Giannetti, "Rainfall map from attenuation data fusion of satellite broadcast and commercial microwave links," *Sensors*, vol. 22, no. 18, 2022, Art. no. 7019, doi: 10.3390/s22187019.

[21] M. Colli et al., "Rainfall fields monitoring based on satellite microwave down-links and traditional techniques in the city of genoa," *IEEE Trans. Geosci. Remote Sens.*, vol. 58, no. 9, pp. 6266–6280, Sep. 2020, doi: 10.1109/TGRS.2020.2976137.

[22] G. Roversi, P. P. Alberoni, A. Fornasiero, and F. Porcù, "Commercial microwave links as a tool for operational rainfall monitoring in northern Italy," *Atmos. Meas. Tech.*, vol. 13, no. 11, pp. 5779–5797, 2020, doi: 10.5194/amt-13-5779-2020.

[23] S. Angeloni et al., "Enhanced estimation of rainfall from opportunistic microwave satellite signals," *IEEE Trans. Geosci. Remote Sens.*, vol. 62, pp. 1–12, 2024, doi: 10.1109/TGRS.2023.3349100.

[24] M. Graf, C. Chwala, J. Polz, and H. Kunstmann, "Rainfall estimation from a German-wide commercial microwave link network:

Optimized processing and validation for 1 year of data," *Hydrol. Earth Syst. Sci.*, vol. 24, no. 6, pp. 2931–2950, 2020, doi: 10.5194/hess-24-2931-2020.

[25] H. Leijnse, R. Uijlenhoet, and J. Stricker, "Hydrometeorological application of a microwave link: 2. precipitation," *Water Resour. Res.*, vol. 43, no. 4, pp. 1–9, 2007, doi: 10.1029/2006WR004989.

[26] F. Giannetti and R. Reggiannini, "Opportunistic rain rate estimation from measurements of satellite downlink attenuation: A survey," *Sensors*, vol. 21, no. 17, 2021, Art. no. 5872, doi: 10.3390/s21175872.

[27] "Guide to instruments and methods of observation (WMO-no. 8)." WMO. Accessed: May, 22, 2025. [Online]. Available: https://community.wmo.int/en/activity-areas/imop/wmo-no_8

[28] C. E. Duchon and C. J. Biddle, "Undercatch of tipping-bucket gauges in high rain rate events," *Adv. Geosci.*, vol. 25, pp. 11–15, Mar. 2010, doi: 10.5194/adgeo-25-11-2010.

[29] A. Cauteruccio, E. Brambilla, M. Stagnaro, L. G. Lanza, and D. Rocchi, "Experimental evidence of the wind-induced bias of precipitation gauges using particle image velocimetry and particle tracking in the wind tunnel," *J. Hydrol.*, vol. 600, Sep. 2021, Art. no. 126690, doi: 10.1016/j.jhydrol.2021.126690.

[30] A. Kruger and W. F. Krajewski, "Two-dimensional video disdrometer: A description," *J. Atmos. Oceanic Technol.*, vol. 19, no. 5, pp. 602–617, 2002, doi: 10.1175/1520-0426(2002)019<0602:TDVDAD>2.0.CO;2.

[31] A. Tokay, D. B. Wolff, and W. A. Petersen, "Evaluation of the new version of the laser-optical disdrometer, OTT parsivel2," *J. Atmos. Oceanic Technol.*, vol. 31, no. 6, pp. 1276–1288, 2014, doi: 10.1175/JTECH-D-13-00174.1.

[32] T. H. Raupach and A. Berne, "Correction of raindrop size distributions measured by Parsivel disdrometers, using a two-dimensional video disdrometer as a reference," *Atmos. Meas. Tech.*, vol. 8, no. 1, pp. 343–365, 2015, doi: 10.5194/amt-8-343-2015.

[33] V. Capozzi, C. Annella, M. Montopoli, E. Adirosi, G. Fusco, and G. Budillon, "Influence of wind-induced effects on laser disdrometer measurements: Analysis and compensation strategies," *Remote Sens.*, vol. 13, no. 15, 2021, Art. no. 3028, doi: 10.3390/rs13153028.

[34] S. Sebastianelli, F. Russo, F. Napolitano, and L. Baldini, "On precipitation measurements collected by a weather radar and a rain gauge network," *Nat. Hazards Earth Syst. Sci.*, vol. 13, no. 3, pp. 605–623, 2013, doi: 10.5194/nhess-13-605-2013.

[35] M. Montopoli, N. Roberto, E. Adirosi, E. Gorgucci, and L. Baldini, "Investigation of weather radar quantitative precipitation estimation methodologies in complex orography," *Atmosphere*, vol. 8, no. 2, 2017, Art. no. 34, doi: 10.3390/atmos8020034.

[36] G. Skofronick-Jackson et al., "The global precipitation measurement (GPM) mission for science and society," *Bull. Amer. Meterol. Soc.*, vol. 98, no. 8, pp. 1679–1695, 2017, doi: 10.1175/BAMS-D-15-00306.1.

[37] R. K. Pradhan et al., "Review of GPM IMERG performance: A global perspective," *Remote Sens. Environ.*, vol. 268, Jan. 2022, Art. no. 112754, doi: 10.1016/j.rse.2021.112754.

[38] E. Adirosi et al., "Validation of GPM rainfall and drop size distribution products through disdrometers in Italy," *Remote Sens.*, vol. 13, no. 11, 2021, Art. no. 2081, doi: 10.3390/rs13112081.

[39] D. Atlas and C. W. Ulbrich, "Path- and area-integrated rainfall measurement by microwave attenuation in the 1–3 cm band," *J. Appl. Meteorol. Climatol.*, vol. 16, no. 12, pp. 1322–1331, 1977, doi: 10.1175/1520-0450(1977)016<1322:PAAIRM>2.0.CO;2.

[40] ITU, *Radio Regulations*. Geneva, Switzerland: ITU, 2020.

[41] A. Ghosh et al., "Millimeter-wave enhanced local area systems: A high-data-rate approach for future wireless networks," *IEEE J. Sel. Areas Commun.*, vol. 32, no. 6, pp. 1152–1163, Jun. 2014, doi: 10.1109/JSAC.2014.2328111.

[42] C. Chwala and H. Kunstmann, "Commercial microwave link networks for rainfall observation: Assessment of the current status and future challenges," *Wiley Interdiscip. Rev.: Water*, vol. 6, no. 2, pp. 1–20, 2019.

[43] M. Colli et al., "A field assessment of a rain estimation system based on satellite-to-earth microwave links," *IEEE Trans. Geosci. Remote Sens.*, vol. 57, no. 5, pp. 2864–2875, May 2019, doi: 10.1109/TGRS.2018.2878338.

[44] F. Giannetti, M. Moretti, R. Reggiannini, and A. Vaccaro, "The NEFOCAST system for detection and estimation of rainfall fields by the opportunistic use of broadcast satellite signals," *IEEE Aerosp. Electron. Syst. Mag.*, vol. 34, no. 6, pp. 16–27, Jun. 2019, doi: 10.1109/MAES.2019.2916292.

[45] M. Fencl et al., "Data formats and standards for opportunistic rainfall sensors," *Open Res. Europe*, vol. 3, Feb. 2024, Art. no. 169, doi: 10.12688/openreseurope.16068.2.

[46] H. Messer and O. Sendik, "A new approach to precipitation monitoring: A critical survey of existing technologies and challenges," *IEEE Signal Process. Mag.*, vol. 32, no. 3, pp. 110–122, May 2015, doi: 10.1109/MSP.2014.2309705.

[47] C. Gianoglio, A. Alyosef, M. Colli, S. Zani, and D. D. Caviglia, "Rain discrimination with machine learning classifiers for opportunistic rain detection system using satellite micro-wave links," *Sensors*, vol. 23, no. 3, 2023, Art. no. 1202, doi: 10.3390/s23031202.

[48] A. Overeem, H. Leijnse, and R. Uijlenhoet, "Retrieval algorithm for rainfall mapping from microwave links in a cellular communication network," *Atmos. Meas. Tech.*, vol. 9, no. 5, pp. 2425–2444, 2016, doi: 10.5194/amt-9-2425-2016.

[49] L. Barthès and C. Mallet, "Rainfall measurement from the opportunistic use of an earth–space link in the KU band," *Atmos. Meas. Tech.*, vol. 6, no. 8, pp. 2181–2193, 2013, doi: 10.5194/amt-6-2181-2013.

[50] C. H. Arslan, K. Aydin, J. V. Urbina, and L. Dyrud, "Satellite-link attenuation measurement technique for estimating rainfall accumulation," *IEEE Trans. Geosci. Remote Sens.*, vol. 56, no. 2, pp. 681–693, Feb. 2018, doi: 10.1109/TGRS.2017.2753045.

[51] "RAINLINK." GitHub. Accessed: Nov. 15, 2024. [Online]. Available: https://github.com/overeem11/RAINLINK

[52] "pycomlink." GitHub. Accessed: Dec. 7, 2024. [Online]. Available: https://github.com/pycomlink/pycomlink

[53] A. Overeem, H. Leijnse, and R. Uijlenhoet, "Measuring urban rainfall using microwave links from commercial cellular

communication networks," *Water Resour. Res.*, vol. 47, no. 12, pp. 1–16, 2011, doi: 10.1029/2010WR010350.

[54] G. Cazzaniga, C. De Michele, M. D'Amico, C. Deidda, A. Ghezzi, and R. Nebuloni, "Hydrological response of a peri-urban catchment exploiting conventional and unconventional rainfall observations: The case study of Lambro catchment," *Hydrol. Earth Syst. Sci. Discuss.*, vol. 26, no. 8, pp. 2093–2111, 2022.

[55] "Smart LNB all-outdoor IoT and satellite CDN terminal." AYECKA. Accessed: Apr. 17, 2024. [Online]. Available: https://www.ayecka.com/smartlnb

[56] N. Blettner, M. Fencl, V. Bareš, H. Kunstmann, and C. Chwala, "Transboundary rainfall estimation using commercial microwave links," *Earth Space Sci.*, vol. 10, no. 8, pp. 1–11, 2023, doi: 10.1029/2023EA002869.

[57] L. W. de Vos, H. Leijnse, A. Overeem, and R. Uijlenhoet, "Quality control for crowdsourced personal weather stations to enable operational rainfall monitoring," *Geophys. Res. Lett.*, vol. 46, no. 15, pp. 8820–8829, 2019, doi: 10.1029/2019GL083731.

[58] J. Polz, M. Graf, and C. Chwala, "Missing rainfall extremes in commercial microwave link data due to complete loss of signal," *Earth Space Sci.*, vol. 10, no. 2, pp. 1–11, 2023, doi: 10.1029/2022EA002456.

[59] M. Schleiss and A. Berne, "Identification of dry and rainy periods using telecommunication microwave links," *IEEE Geosci. Remote Sens. Lett.*, vol. 7, no. 3, pp. 611–615, Jul. 2010, doi: 10.1109/LGRS.2010.2043052.

[60] J. Polz, C. Chwala, M. Graf, and H. Kunstmann, "Rain event detection in commercial microwave link attenuation data using convolutional neural networks," *Atmos. Meas. Tech.*, vol. 13, no. 7, pp. 3835–3853, 2020, doi: 10.5194/amt-13-3835-2020.

[61] J. Pudashine et al., "Deep learning for an improved prediction of rainfall retrievals from commercial microwave links," *Water Resour. Res.*, vol. 56, no. 7, 2020, Art. no. WR026255, doi: 10.1029/2019WR026255.

[62] P. Zhang, X. Liu, and K. Pu, "Classification of dry and wet periods using commercial microwave links: A one-class classification machine learning approach based on autoencoders," *IEEE Trans. Geosci. Remote Sens.*, vol. 62, pp. 1–13, 2023, doi: 10.1109/TGRS.2023.3339682.

[63] J. Ostrometzky and H. Messer, "Dynamic determination of the baseline level in microwave links for rain monitoring from minimum attenuation values," *IEEE J. Sel. Topics Appl. Earth Observ. Remote Sens.*, vol. 11, no. 1, pp. 24–33, Jan. 2018, doi: 10.1109/JSTARS.2017.2752902.

[64] T. Van Het Schip, A. Overeem, H. Leijnse, R. Uijlenhoet, J. Meirink, and A. van Delden, "Rainfall measurement using cell phone links: Classification of wet and dry periods using geostationary satellites," *Hydrological Sci. J.*, vol. 62, no. 9, pp. 1343–1353, 2017, doi: 10.1080/02626667.2017.1329588.

[65] M. Graf et al., "Improved rain event detection in commercial microwave link time series via combination with MSG SEVIRI data," *Atmos. Meas. Tech.*, vol. 17, no. 7, pp. 2165–2182, 2024, doi: 10.5194/amt-17-2165-2024.

[66] J. Ostrometzky, G. Rafalovich, B. Kagan, and H. Messer, "Standalone, affordable IoT satellite terminals and their opportunistic use for rain monitoring," *IEEE Internet Things Mag.*, vol. 5, no. 4, pp. 100–105, Dec. 2022, doi: 10.1109/IOTM.001.2200166.

[67] M. Xian, X. Liu, M. Yin, K. Song, S. Zhao, and T. Gao, "Rainfall monitoring based on machine learning by earth-space link in the KU band," *IEEE J. Sel. Topics Appl. Earth Observ. Remote Sens.*, vol. 13, pp. 3656–3668, 2020, doi: 10.1109/JSTARS.2020.3004375.

[68] R. A. Giro, L. Luini, C. G. Riva, D. Pimienta-del Valle, and J. M. R. Salis, "Real-time rainfall estimation using satellite signals: Development and assessment of a new procedure," *IEEE Trans. Instrum. Meas.*, vol. 71, pp. 1–10, 2022, doi: 10.1109/TIM.2022.3165840.

[69] B. He, X. Liu, S. Hu, K. Song, and T. Gao, "Use of the c-band microwave link to distinguish between rainy and dry periods," *Adv. Meteorol.*, vol. 2019, pp. 1–9, Jul. 2019.

[70] C. Gianoglio, M. Colli, S. Zani, and D. D. Caviglia, "An online training procedure for rain detection models applied to satellite microwave links," *IEEE Geosci. Remote Sens. Lett.*, vol. 20, pp. 1–5, 2023, doi: 10.1109/LGRS.2023.3328718.

[71] C. Gianoglio, S. Zani, M. Colli, and D. D. Caviglia, "Rainfall classification in genoa: Machine learning vs. adaptive statistical models using satellite microwave links," *IEEE Access*, vol. 12, pp. 132,744–132,753, 2024, doi: 10.1109/ACCESS.2024.3458407.

[72] J. D. Parsons, *The Mobile Radio Propagation Channel*, 2nd ed. Hoboken, NJ, USA: Wiley, 2001.

[73] F. Fenicia et al., "Microwave links for rainfall estimation in an urban environment: Insights from an experimental setup in Luxembourg-City," *J. Hydrol.*, vols. 464–465, pp. 69–78, Sep. 2012, doi: 10.1016/j.jhydrol.2012.06.047.

[74] "Propagation data and prediction methods required for the design of earth-space telecommunication systems," Int. Telecommun. Union, Geneva, Switzerland, Tech. Rep. ITU-R P.618-13, 2017.

[75] E. Adirosi et al., "Evaluation of rainfall estimation derived from commercial interactive DVB receivers using disdrometer, rain gauge, and weather radar," *IEEE Trans. Geosci. Remote Sens.*, vol. 59, no. 11, pp. 8978–8991, Nov. 2021, doi: 10.1109/TGRS.2020.3041448.

[76] M. Kikuchi and K. Suzuki, "Characterizing vertical particle structure of precipitating cloud system from multiplatform measurements of a-train constellation," *Geophys. Res. Lett.*, vol. 46, no. 2, pp. 1040–1048, 2019, doi: 10.1029/2018GL081244.

[77] R. Raich, P. Alpert, and H. Messer, "Vertical precipitation estimation using microwave links in conjunction with weather radar," *Environments*, vol. 5, no. 7, 2018, Art. no. 74, doi: 10.3390/environments5070074.

[78] R. Olsen, D. Roger, and D. Hodge, "The aRb relation in the calculation of rain attenuation," *IEEE Trans. Antennas Propag.*, vol. 26, no. 2, pp. 318–329, Mar. 1978, doi: 10.1109/TAP.1978.1141845.

[79] "Specific attenuation model for rain for use in prediction methods," Int. Telecommun. Union, Geneva, Switzerland, Tech. Rep., ITU-R P.838-3, 2005.

[80] E. Adiosi et al., "Exploiting satellite Ka and Ku links for the real-time estimation of rain intensity," in *Proc. 32nd General*

Assem. Sci. Symp. Int. Union Radio Sci. (URSI GASS), Montreal, QC, Canada, Aug. 2017, pp. 1–4, doi: 10.23919/URSI-GASS.2017.8105128.

[81] R. Nebuloni, G. Cazzaniga, M. D'Amico, C. Deidda, and C. De Michele, "Comparison of cml rainfall data against rain gauges and disdrometers in a mountainous environment," *Sensors*, vol. 22, no. 9, 2022, Art. no. 3218, doi: 10.3390/s22093218.

[82] "Rain height model for prediction methods," Int. Telecommun. Union, Geneva, Switzerland, Tech. Rep. ITU-R P.839-4, 2013.

[83] A. Kumar, J. Dudhia, R. Rotunno, D. Niyogi, and U. C. Mohanty, "Analysis of the 26 July 2005 heavy rain event over Mumbai, India using the weather research and forecasting (WRF) model," *Q. J. R. Meteorolog. Soc.*, vol. 134, no. 636, pp. 1897–1910, 2008, doi: 10.1002/qj.325.

[84] "High resolution model." ECMWF. Accessed: Nov. 15, 2024. [Online]. Available: https://www.ecmwf.int/en/forecasts/datasets/set-i

[85] H. Leijnse, R. Uijlenhoet, and J. Stricker, "Microwave link rainfall estimation: Effects of link length and frequency, temporal sampling, power resolution, and wet antenna attenuation," *Adv. Water Resour.*, vol. 31, no. 11, pp. 1481–1493, 2008, doi: 10.1016/j.advwatres.2008.03.004.

[86] A. Zinevich, H. Messer, and P. Alpert, "Prediction of rainfall intensity measurement errors using commercial microwave communication links," *Atmos. Meas. Tech.*, vol. 3, no. 5, pp. 1385–1402, 2010, doi: 10.5194/amt-3-1385-2010.

[87] A. Ishimaru, *Electromagnetic Wave Propagation, Radiation, and Scattering: From Fundamentals to Applications*. Hoboken, NJ, USA: Wiley, 2017.

[88] T. Oguchi, "Electromagnetic wave propagation and scattering in rain and other hydrometeors," *Proc. IEEE*, vol. 71, no. 9, pp. 1029–1078, Sep. 1983, doi: 10.1109/PROC.1983.12724.

[89] C. Capsoni, F. Fedi, and A. Paraboni, "A comprehensive meteorologically oriented methodology for the prediction of wave propagation parameters in telecommunication applications beyond 10 GHz," *Radio Sci.*, vol. 22, no. 3, pp. 387–393, May/Jun. 1987, doi: 10.1029/RS022i003p00387.

[90] H. E. Green, "Propagation impairment on Ka-band satcom links in tropical and equatorial regions," *IEEE Antennas Propag. Mag.*, vol. 46, no. 2, pp. 31–45, Apr. 2004, doi: 10.1109/MAP.2004.1305532.

[91] "Attenuation by atmospheric gases and related effects," Int. Telecommun. Union, Geneva, Switzerland, Tech. Rep. ITU-R P.676-13, 2022.

[92] "Attenuation due to clouds and fog," Int. Telecommun. Union, Geneva, Switzerland, Tech. Rep. ITU-R P.840-9, 2023.

[93] "Propagation data and prediction methods required for the design of terrestrial line-of-sight systems," Int. Telecommun. Union, Geneva, Switzerland, Tech. Rep. ITU-R P.530-18, 2021.

[94] S. Noreen, F. Giannetti, and V. Lottici, "Earth and Martian sand and dust storms: A comprehensive review of attenuation modelling and measurements," *IEEE Access*, vol. 12, pp. 878–922, 2024, doi: 10.1109/ACCESS.2023.3347489.

[95] F. Marzano, G. Vulpiani, and W. Rose, "Microphysical characterization of microwave radar reflectivity due to volcanic ash clouds," *IEEE Trans. Geosci. Remote Sens.*, vol. 44, no. 2, pp. 313–327, Feb. 2006, doi: 10.1109/TGRS.2005.861010.

[96] "Propagation data required for the evaluation of interference between stations in space and those on the surface of the earth," Int. Telecommun. Union, Geneva, Switzerland, Tech. Rep. ITU-R P.619-5, 2021.

[97] M. Singh, S. Hassan, M. Ain, K. Igarashi, K. Tanaka, and M. Iida, "Analysis of tropospheric scintillation intensity on earth to space in Malaysia," *Amer. J. Appl. Sci.*, vol. 3, no. 9, pp. 2029–2032, 2006, doi: 10.3844/ajassp.2006.2029.2032.

[98] "Reference standard atmospheres," Int. Telecommun. Union, Geneva, Switzerland, Tech. Rep. ITU-R P.835-6, 2017.

[99] D. Cherkassky, J. Ostrometzky, and H. Messer, "Precipitation classification using measurements from commercial microwave links," *IEEE Trans. Geosci. Remote Sens.*, vol. 52, no. 5, pp. 2350–2356, May 2014, doi: 10.1109/TGRS.2013.2259832.

[100] K. Paulson and A. Al-Mreri, "A rain height model to predict fading due to wet snow on terrestrial links," *Radio Sci.*, vol. 46, no. 4, pp. 1–6, 2011, doi: 10.1029/2010RS004555.

[101] E. A. A. Elsheikh, M. R. Islam, M. H. Habaebi, A. F. Ismail, and A. Zyoud, "Dust storm attenuation modeling based on measurements in Sudan," *IEEE Trans. Antennas Propag.*, vol. 65, no. 8, pp. 4200–4208, Aug. 2017, doi: 10.1109/TAP.2017.2715369.

[102] M. Mehmood, S. Saleem, and R. Filjar, "Eyjafjallajökull volcanic ash 2010 effects on GPS positioning performance in the Adriatic Sea region," *Atmosphere*, vol. 13, no. 1, 2022, Art. no. 47, doi: 10.3390/atmos13010047.

[103] M. Kharadly and R. Ross, "Effect of wet antenna attenuation on propagation data statistics," *IEEE Trans. Antennas Propag.*, vol. 49, no. 8, pp. 1183–1191, Aug. 2001, doi: 10.1109/8.943313.

[104] M. Schleiss, J. Rieckermann, and A. Berne, "Quantification and modeling of wet-antenna attenuation for commercial microwave links," *IEEE Geosci. Remote Sens. Lett.*, vol. 10, no. 5, pp. 1195–1199, Sep. 2013, doi: 10.1109/LGRS.2012.2236074.

[105] J. M. Garcia-Rubia, J. M. Riera, A. Benarroch, and P. Garcia-del Pino, "Estimation of rain attenuation from experimental drop size distributions," *IEEE Antennas Wireless Propag. Lett.*, vol. 10, pp. 839–842, 2011, doi: 10.1109/LAWP.2011.2163609.

[106] P. Valtr, M. Fencl, and V. Bareš, "Excess attenuation caused by antenna wetting of terrestrial microwave links at 32 GHz," *IEEE Antennas Wireless Propag. Lett.*, vol. 18, no. 8, pp. 1636–1640, Aug. 2019, doi: 10.1109/LAWP.2019.2925455.

[107] M. Rytir and J. Sander, "Attenuation due to snow accumulation on antenna at Ka-band; effect and mitigation techniques," in *Proc. 25th Ka Broadband Commun. Conf.*, Sep./Oct. 2019, pp. 1–9.

[108] F. Sapienza et al., "Performance comparison of different types of broadcast satellite receivers for opportunistic rain estimation," in *Proc. 2024 4th URSI Atlantic Radio Sci. Meeting (AT-RASC)*, Meloneras, Spain, May 2024, pp. 1–4.

[109] U. Mankong et al., "Millimeter wave attenuation due to wind and heavy rain in a tropical region," *Sensors*, vol. 23, no. 5, 2023, Art. no. 2532, doi: 10.3390/s23052532.

[110] J. C. M. Andersson, J. Olsson, R. C. Z. van de Beek, and J. Hansryd, "OpenMRG: Open data from microwave links, radar, and gauges for rainfall quantification in Gothenburg, Swe-

den," *Earth Syst. Sci. Data*, vol. 14, no. 12, pp. 5411–5426, 2022, doi: 10.5194/essd-14-5411-2022.

[111] G. Maral, M. Bousquet, and Z. Sun, *Satellite Communications Systems: Systems, Techniques and Technology*. Hoboken, NJ, USA: Wiley, 2020.

[112] P. Fortescue, G. Swinerd, and J. Stark, *Spacecraft Systems Engineering*. Hoboken, NJ, USA: Wiley, 2011.

[113] D. M. Stoian Borissov and Y. Wu, "East–west geo satellite station-keeping with degraded thruster response," *Feature Papers Aerosp.*, vol. 2, no. 4, pp. 581–601, 2015, doi: 10.3390/aerospace2040581.

[114] F. Sapienza, F. Giannetti, and A. Vaccaro, "A poor's man approach to solar radio emission characterization," in *Proc. 4th URSI Atlantic Radio Sci. Meeting (AT-RASC)*, Meloneras, Spain, May 2024, pp. 1–4.

[115] "SurfBeam 2 residential satellite terminal." VIASAT. Accessed: Sep. 21, 2024. [Online]. Available: http://visat.bg/sites/default/files/ViaSat_Surfbeam2_terminal_Datasheet.pdf

[116] "KONNECT." konnect.com. Accessed: Sep. 21, 2024. [Online]. Available: https://konnect.com/

[117] F. Giannetti, M. Moretti, R. Reggiannini, A. Vaccaro, S. Scarfone, and A. Ortolani, "On the opportunistic use of commercial Ku and Ka band satcom networks for rain rate estimation: Potentials and critical issues," in *Proc. IEEE Int. Conf. Acoust., Speech Signal Process. (ICASSP)*, Barcelona, Spain, 2020, pp. 9011–9015, doi: 10.1109/ICASSP40776.2020.9053668.

[118] A. Eshel, H. Messer, H. Kunstmann, P. Alpert, and C. Chwala, "Quantitative analysis of the performance of spatial interpolation methods for rainfall estimation using commercial microwave links," *J. Hydrometeorol.*, vol. 22, no. 4, pp. 831–843, 2021, doi: 10.1175/JHM-D-20-0164.1.

[119] S. H. Lin, "11-GHz radio: Nationwide long-term rain rate statistics and empirical calculation of 11-GHz microwave rain attenuation," *Bell System Tech. J.*, vol. 56, no. 9, pp. 1581–1604, Nov. 1977, doi: 10.1002/j.1538-7305.1977.tb00582.x.

[120] L. da Silva Mello, M. Pontes, R. de Souza, and N. P. García, "Prediction of rain attenuation in terrestrial links using full rainfall rate distribution," *Electron. Lett.*, vol. 43, no. 25, pp. 1442–1443, 2007, doi: 10.1049/el:20072410.

[121] G. Bryant, I. Adimula, C. Riva, and G. Brussaard, "Rain attenuation statistics from rain cell diameters and heights," *Int. J. Satell. Commun.*, vol. 19, no. 3, pp. 263–283, 2001, doi: 10.1002/sat.673.

[122] A. Rayitsfeld, R. Samuels, A. Zinevich, U. Hadar, and P. Alpert, "Comparison of two methodologies for long term rainfall monitoring using a commercial microwave communication system," *Atmos. Res.*, vols. 104–105, pp. 119–127, Feb. 2012, doi: 10.1016/j.atmosres.2011.08.011.

[123] A. Overeem, H. Leijnse, and R. Uijlenhoet, "Country-wide rainfall maps from cellular communication networks," *Proc. Natl. Acad. Sci.*, vol. 110, no. 8, pp. 2741–2745, 2013, doi: 10.1073/pnas.1217961110.

[124] M. F. Rios Gaona, A. Overeem, H. Leijnse, and R. Uijlenhoet, "Measurement and interpolation uncertainties in rainfall maps from cellular communication networks," *Hydrol. Earth Syst. Sci.*, vol. 19, no. 8, pp. 3571–3584, 2015, doi: 10.5194/hess-19-3571-2015.

[125] A. Zinevich, H. Messer, and P. Alpert, "Frontal rainfall observation by a commercial microwave communication network," *J. Appl. Meteorol. Climatol.*, vol. 48, no. 7, pp. 1317–1334, 2009, doi: 10.1175/2008JAMC2014.1.

[126] A. Zinevich, P. Alpert, and H. Messer, "Estimation of rainfall fields using commercial microwave communication networks of variable density," *Adv. Water Resour.*, vol. 31, no. 11, pp. 1470–1480, 2008, doi: 10.1016/j.advwatres.2008.03.003.

[127] M. D'Amico, A. Manzoni, and G. L. Solazzi, "Use of operational microwave link measurements for the tomographic reconstruction of 2-D maps of accumulated rainfall," *IEEE Geosci. Remote Sens. Lett.*, vol. 13, no. 12, pp. 1827–1831, Dec. 2016, doi: 10.1109/LGRS.2016.2614326.

[128] F. Sapienza et al., "A feasibility study on opportunistic rainfall measurement from satellite TV broadcasts," URSI Radio Sci. Lett., vol. 4, pp. 1–4, 2020. [Online]. Available: https://www.ursi.org/Publications/RadioScienceLetters/Volume4/RSL22-0033.pdf

[129] F. Sapienza, F. Giannetti, G. Manara, G. Bacci, and A. Vaccaro, "The potential of opportunistic rainfall sensing to complement conventional sensors: The 2017 flash flood in Leghorn (Italy) as a case study," in *Proc. URSI Asia-Pacific Radio Sci. Conf.*, Sidney, Australia, 2025.

[130] F. Sapienza et al., "Rainfall field reconstruction by opportunistic use of the rain-induced attenuation on microwave satellite signals: The July 2021 extreme rain event in Germany as a case study," in *Proc. 2nd IEEE Ukrainian Microw. Week (UkrMW)*, Ukraine, 2022, pp. 523–528, doi: 10.1109/UkrMW58013.2022.10037149.

[131] F. Sapienza, F. Giannetti, E. Adirosi, and L. Baldini, "Precipitation field reconstruction and tracking using opportunistic rain sensors: the summer 2021 catastrophic event in Germany as a case study," in *Proc. Int. Conf. Opportunistic Sens. Precipitation - OpenSense*, Offenbach, Germany, 2025.

[132] A. Ortolani, F. Caparrini, S. Melani, L. Baldini, and F. Giannetti, "An enkf-based method to produce rainfall maps from simulated satellite-to-ground mw-link signal attenuation," *J. Hydrometeorol.*, vol. 22, no. 5, pp. 1333–1350, 2021, doi: 10.1175/JHM-D-20-0128.1.

[133] R. Nebuloni, M. D'Amico, G. Cazzaniga, and C. De Michele, "On the use of minimum and maximum attenuation for retrieving rainfall intensity through commercial microwave links," *URSI Radio Sci. Lett.*, vol. 2, pp. 1–4, 2020. [Online]. Available: https://www.ursi.org/Publications/RadioScienceLetters/Volume2/RSL20-0062.pdf

[134] A. Dissanayake and N. McEwan, "Radar and attenuation properties of rain and bright band," in *Proc. Int. Conf. Antennas Propag.*, London, England, pp. 125–129., 1978.

[135] C. Chwala, F. Keis, and H. Kunstmann, "Real-time data acquisition of commercial microwave link networks for hydrometeorological applications," *Atmos. Meas. Tech.*, vol. 9, no. 3, pp. 991–999, 2016, doi: 10.5194/amt-9-991-2016.

[136] L. Luini, G. Roveda, M. Zaffaroni, M. Costa, and C. G. Riva, "The impact of rain on short *E*-band radio links for 5G

mobile systems: Experimental results and prediction models," *IEEE Trans. Antennas Propag.*, vol. 68, no. 4, pp. 3124–3134, Apr. 2020, doi: 10.1109/TAP.2019.2957116.

[137] F. Giannetti, A. Vaccaro, F. Sapienza, G. Bacci, V. Lottici, and L. Baldini, "Multi-satellite rain sensing: Design criteria and implementation issues," in *Proc. 3rd URSI Atlantic Asia Pacific Radio Sci. Meeting (AT-AP-RASC)*, Gran Canaria, Spain, 2022, pp. 1–4, doi: 10.23919/AT-AP-RASC54737.2022.9814405.

[138] B. Haese, S. Hörning, C. Chwala, A. Bárdossy, B. Schalge, and H. Kunstmann, "Stochastic reconstruction and interpolation of precipitation fields using combined information of commercial microwave links and rain gauges," *Water Resour. Res.*, vol. 53, no. 12, pp. 10,740–10,756, 2017, doi: 10.1002/2017WR021015.

[139] J. Pastorek, M. Fencl, J. Rieckermann, and V. Bareš, "Precipitation estimates from commercial microwave links: Practical approaches to wet-antenna correction," *IEEE Trans. Geosci. Remote Sens.*, vol. 60, pp. 1–9, 2022, doi: 10.1109/TGRS.2021.3110004.

[140] S. Puca et al., "The validation service of the hydrological saf geostationary and polar satellite precipitation products," *Nat. Hazards Earth Syst. Sci.*, vol. 14, no. 4, pp. 871–889, 2014, doi: 10.5194/nhess-14-871-2014.

[141] M. Hossin and M. N. Sulaiman, "A review on evaluation metrics for data classification evaluations," *Int. J. Data Mining Knowl. Manage. Process*, vol. 5, no. 2, pp. 1–11, 2015, doi: 10.5121/ijdkp.2015.5201.

[142] C.-C. Wang, "On the calculation and correction of equitable threat score for model quantitative precipitation forecasts for small verification areas: The example of Taiwan," *Weather Forecasting*, vol. 29, no. 4, pp. 788–798, 2014, doi: 10.1175/WAF-D-13-00087.1.

[143] H. V. Habi and H. Messer, "Wet-dry classification using LSTM and commercial microwave links," in *Proc. IEEE 10th Sensor Array Multichannel Signal Process. Workshop (SAM)*, Sheffield, U.K., 2018, pp. 149–153, doi: 10.1109/SAM.2018.8448679.

[144] N. Blettner, C. Chwala, B. Haese, S. Hörning, and H. Kunstmann, "Combining commercial microwave link and rain gauge observations to estimate countrywide precipitation: A stochastic reconstruction and pattern analysis approach," *Water Resour. Res.*, vol. 58, no. 10, pp. 1–16, 2022, doi: 10.1029/2022WR032563.

[145] M. Fencl, J. Rieckermann, P. Sýkora, D. Stránský, and V. Bareš, "Commercial microwave links instead of rain gauges: Fiction or reality?," *Water Sci. Technol.*, vol. 71, no. 1, pp. 31–37, 2014, doi: 10.2166/wst.2014.466.

[146] A. Overeem, H. Leijnse, and R. Uijlenhoet, "Two and a half years of country-wide rainfall maps using radio links from commercial cellular telecommunication networks," *Water Resour. Res.*, vol. 52, no. 10, pp. 8039–8065, 2016, doi: 10.1002/2016WR019412.

[147] L. W. de Vos, A. Overeem, H. Leijnse, and R. Uijlenhoet, "Rainfall estimation accuracy of a nationwide instantaneously sampling commercial microwave link network: Error dependency on known characteristics," *J. Atmos. Oceanic Technol.*, vol. 36, no. 7, pp. 1267–1283, 2019, doi: 10.1175/JTECH-D-18-0197.1.

[148] G. Gragnani, M. Colli, E. Tavanti, and D. Caviglia, "Advanced real-time monitoring of rainfall using commercial satellite broadcasting service: A case study," *Sensors*, vol. 21, no. 3, 2021, Art. no. 691, doi: 10.3390/s21030691.

[149] G. Scognamiglio et al., "Deep learning for opportunistic rain estimation via satellite microwave links," *Sensors*, vol. 24, no. 21, 2024, Art. no. 6944, doi: 10.3390/s24216944.

[150] F. D. Diba, M. A. Samad, J. Ghimire, and D.-Y. Choi, "Wireless telecommunication links for rainfall monitoring: Deep learning approach and experimental results," *IEEE Access*, vol. 9, pp. 66,769–66,780, 2021, doi: 10.1109/ACCESS.2021.3076781.

[151] E. Øydvin, M. Graf, C. Chwala, M. A. Wolff, N.-O. Kitterød, and V. Nilsen, "Technical note: A simple feedforward artificial neural network for high-temporal-resolution rain event detection using signal attenuation from commercial microwave links," *Hydrol. Earth Syst. Sci.*, vol. 28, no. 23, pp. 5163–5171, 2024, doi: 10.5194/hess-28-5163-2024.

[152] "Ericsson microwave outlook," Ericsson, Stockholm, Sweden, Rep. no. EAB-18:012818 Uen, 2018. [Online]. Available: https://www.ericsson.com/en/reports-and-papers/microwave-outlook/reports/2018

[153] M. Fencl, M. Dohnal, P. Valtr, M. Grabner, and V. Bareš, "Atmospheric observations with e-band microwave links – Challenges and opportunities," *Atmos. Meas. Tech.*, vol. 13, no. 12, pp. 6559–6578, 2020, doi: 10.5194/amt-13-6559-2020.

[154] O. Kodheli et al., "Satellite communications in the new space era: A survey and future challenges," *IEEE Commun. Surveys Tuts.*, vol. 23, no. 1, pp. 70–109, 1st Quart. 2021, doi: 10.1109/COMST.2020.3028247.

[155] R. A. Giro, L. Luini, and C. G. Riva, "Rainfall estimation from tropospheric attenuation affecting satellite links," *Information*, vol. 11, no. 1, 2020, Art. no. 11, doi: 10.3390/info11010011.

[156] I. Leyva-Mayorga et al., "Leo small-satellite constellations for 5G and beyond-5G communications," *IEEE Access*, vol. 8, pp. 184,955–184,964, 2020, doi: 10.1109/ACCESS.2020.3029620.

[157] T. Ma, B. Qian, X. Qin, X. Liu, H. Zhou, and L. Zhao, "Satellite-terrestrial integrated 6G: An ultra-dense LEO networking management architecture," *IEEE Wireless Commun.*, vol. 31, no. 1, pp. 62–69, Feb. 2024, doi: 10.1109/MWC.011.2200198.

[158] "Non-terrestrial networks." 3GPP. Accessed: May 14, 2024. [Online]. Available: https://www.3gpp.org/technologies/ntn-overview

[159] S. Cakaj, "Rain attenuation impact on performance of satellite ground stations for low earth orbiting (LEO) satellites in Europe," *Int. J. Commun., Netw. Syst. Sci.*, vol. 02, no. 6, pp. 480–485, 2009, doi: 10.4236/ijcns.2009.26052.

[160] X. Shen, D. D. Huang, B. Song, C. Vincent, and R. Togneri, "3-D tomographic reconstruction of rain field using microwave signals from LEO satellites: Principle and simulation results," *IEEE Trans. Geosci. Remote Sens.*, vol. 57, no. 8, pp. 5434–5446, Aug. 2019, doi: 10.1109/TGRS.2019.2899391.

GRS